Chapter 2

Enabling Theory

As seen in the previous chapter, we wish to predict which reaction products form when a particular alloy is exposed to a given gas, and the effects of temperature and pressure on the outcome. This requires the use of chemical thermodynamics, and in particular the use of phase equilibria. The rates at which the products form are usually governed by diffusion and interfacial processes, both involving crystallographic defects. Finally, the structural integrity of any solid is determined by its mechanical state. We now review these areas, focusing on their application to high temperature oxidation reactions.

2.1 CHEMICAL THERMODYNAMICS

The question of whether or not an oxide is formed is answered by determining the most stable state of the reacting system

$$\mathrm{M} + \frac{1}{2}\mathrm{O}_2 = \mathrm{MO} \qquad [2.1]$$

At a constant temperature and pressure the stability of a system is measured by its Gibbs free energy. The total Gibbs free energy, G, of a system is defined as

$$G = H - TS = U + pV - TS \qquad [2.2]$$

where H is the enthalpy, S the entropy, U the internal energy, V the volume of the system and p, T have their usual meanings. For a system in which compositional change through chemical reaction is possible, the reversible internal energy change is provided by the basic laws of thermodynamics

$$dU = TdS - pdV + \sum_i \mu_i dn_i \qquad [2.3]$$

where n_i is the number of moles of component i, the summation is over all components in the system and

$$\mu_i = \left(\frac{\partial U}{\partial n_i}\right)_{T,P,n_{j\neq i}} \qquad [2.4]$$

High Temperature Oxidation and Corrosion of Metals. http://dx.doi.org/10.1016/B978-0-08-100101-1.00002-9

is the *chemical potential*. Combination of the differential form of Eq. [2.2] with Eq. [2.3] yields

$$dG = Vdp - SdT + \sum_i \mu_i dn_i \qquad [2.5]$$

An isothermal, isobaric system is at equilibrium where G is the minimum, the location of which is determined by the differential

$$dG = 0 \qquad [2.6]$$

Under these conditions, it is seen that the partial molar free energy of a component

$$\overline{G}_i = \left(\frac{\partial G}{\partial n_i}\right)_{T,P,n_{j\neq i}} = \mu_i \qquad [2.7]$$

is equivalent to its chemical potential. The overbar symbol will be used to denote partial molar quantities in general. Integration of Eq. [2.5] leads to

$$G = \sum_i \mu_i n_i \qquad [2.8]$$

when $dT = 0 = dp$, and a combination of Eqs [2.6] and [2.8] yields the condition for chemical equilibrium

$$\sum_i n_i \mu_i = 0 \qquad [2.9]$$

which is the Gibbs equation. To utilise this result, it is necessary to evaluate the μ_i in terms of compositional variables.

2.1.1 Chemical Potential and Composition

For an isothermal system of fixed composition, application of Eq. [2.5] to component A yields

$$\frac{\partial \overline{G}_A}{\partial p} = \overline{V}_A \qquad [2.10]$$

where $\overline{V}_A$ is the partial molar volume. The latter is found for a perfect gas mixture to be

$$\overline{V}_A = \frac{V}{\sum_i n_i} = \frac{N_A RT}{p_A} \qquad [2.11]$$

where $N_A = n_A / \sum_i n_i$ is the mole fraction. Rewriting Eq. [2.10] as an exact differential and substituting from Eq. [2.11], it is found that

$$d\mu_A = d\overline{G}_A = \frac{N_A RT}{p_A} dp \qquad [2.12]$$

Further substitution from Dalton's law of partial pressures

$$p_A/p = N_A; \quad dp_A = N_A dp$$

then leads to

$$d\mu = RT\frac{dp_A}{p_A} \tag{2.13}$$

which upon integration yields

$$\mu = \mu^\circ + RT\ln\frac{p_A}{p_A^\circ} \tag{2.14}$$

Here the arbitrarily chosen value $p_A = p_A^\circ$ is used to define the standard state at which the chemical potential has its standard (temperature dependent) value of μ°. It is convenient to choose p_A° as unity, commonly 1 atm.

2.1.2 Chemical Equilibrium in Gas Mixtures

We consider reactions such as

$$CO_2 = CO + \frac{1}{2}O_2 \tag{2.15}$$

$$H_2O = H_2 + \frac{1}{2}O_2 \tag{2.16}$$

with the intention of calculating p_{O_2}. More generally, any reaction can be formulated as a summation over all chemical species involved

$$0 = \sum_i \Sigma\nu_i M_i \tag{2.17}$$

where the M_i are the symbols for the different chemical species (CO, CO_2, etc.) and the ν_i are the stoichiometric coefficients, which are negative for reactants and positive for products. Thus for reaction Eq. [2.15] $\nu_1 = -1$, $\nu_2 = 1$ and $\nu_3 = 0.5$, it follows that

$$\frac{dn_1}{\nu_1} = \frac{dn_2}{\nu_2} = \frac{dn_3}{\nu_3}\cdots = \frac{dn_m}{\nu_m} = d\xi \tag{2.18}$$

where again ξ denotes the extent of reaction. Eq. [2.5] may now be written

$$\begin{aligned} dG &= Vdp - SdT + \mu_A dn_A + \cdots \mu_m dn_m \\ &= Vdp - SdT + (\nu_A\mu_A + \cdots \nu_m\mu_m)d\xi \end{aligned}$$

and hence

$$(\partial G/\partial\xi)_{T,P} = \sum_i \nu_i\mu_i \tag{2.19}$$

The condition for chemical equilibrium is therefore given by Eq. [2.9] in the specific form

$$\sum_i \nu_i \mu_i = 0 \qquad [2.20]$$

Substituting from Eq. [2.14], we find in the case of the CO_2 reaction [2.15]

$$0 = \mu^\circ_{CO} + 0.5\mu^\circ_{O_2} - \mu^\circ_{CO_2} + RT \ln \frac{p_{CO} p_{O_2}^{\frac{1}{2}}}{p_{CO_2}} \qquad [2.21]$$

Recognising that the standard chemical potentials are, by definition, the standard free energies per unit mole, this result is recast as

$$\mu^\circ_{CO} + 0.5\mu^\circ_{O_2} - \mu^\circ_{CO_2} = \Delta G^\circ = -RT \ln \frac{p_{CO} p_{O_2}^{\frac{1}{2}}}{p_{CO_2}} \qquad [2.22]$$

where $\Delta G^\circ = \mu^\circ_{CO} + 0.5\mu^\circ_{O_2} - \mu^\circ_{CO_2}$ is termed the standard free energy change. Since ΔG° is a function only of temperature, the quantity K_p, called the equilibrium constant at fixed total pressure,

$$K_p = \exp(-\Delta G^\circ / RT) = \frac{p_{CO} p_{O_2}^{\frac{1}{2}}}{p_{CO_2}} \qquad [2.23]$$

is also a function only of temperature. Tabulated values of ΔG° are available [1–3], allowing easy calculation of K_p. A small selection of useful values is provided in Table 2.1. If the equilibrium ratio p_{CO}/p_{CO_2} is known, then the oxygen partial pressure is readily found from Eq. [2.23].

A more commonly encountered problem is that of calculating p_{O_2} from a knowledge of the input gas composition, ie, before equilibrium is reached. This is dealt with using the stoichiometry of the reaction, and specifying an unknown extent of reaction to be determined. If there is initially no oxygen present and the input gas mixture consists of a moles of CO_2 plus b moles of CO, we see that $\frac{x}{2}$ moles of O_2 are formed with the consumption of x moles of CO_2 and the generation of x moles of CO

$$\begin{array}{ccccc} CO_2 & = & CO & + & \frac{1}{2}O_2 \\ (a-x) & & (b+x) & & \frac{x}{2} \end{array}$$

In this system, $\sum_i n_i = a + b + \frac{x}{2}$, and the partial pressures are given by

$$p_i = \frac{n_i}{a + b + x/2} p \qquad [2.24]$$

TABLE 2.1 Standard Free Energies[a] of Reaction [1,2]

	$\Delta G^\circ = A + B$ (J mol^{-1})	
Reaction	*A*	*B*
$\frac{2}{3}Al(l) + \frac{1}{2}O_2 = \frac{1}{3}Al_2O_3$	−565,900	128
$\frac{1}{2}Si + \frac{1}{2}O_2 = \frac{1}{2}SiO_2$	−451,040	86.8
$Mn + \frac{1}{2}O_2 = MnO$	−412,304	72.8
$Zn + \frac{1}{2}O_2 = ZnO$	−356,190	107.9
$\frac{2}{3}Cr + \frac{1}{2}O_2 = \frac{1}{3}Cr_2O_3$	−373,420	86
$\frac{23}{6}Cr + C = \frac{1}{6}Cr_{23}C_6$	−68,533	−6.45
$\frac{7}{27}Cr_{23}C_6 + C = \frac{23}{27}Cr_7C_3$	−42,049	−11.9
$\frac{3}{5}Cr_7C_3 + C = \frac{7}{5}Cr_3C_2$	−13,389	−0.84
$2Cr + \frac{1}{2}N_2 = Cr_2N$	−108,575	138
$Cr_2N + \frac{1}{2}N_2 = 2CrN$	−133,890	174
$Fe + \frac{1}{2}O_2 = FeO$	−264,890	65.4
$3FeO + \frac{1}{2}O_2 = Fe_3O_4$	−312,210	125.1
$2Fe_3O_4 + \frac{1}{2}O_2 = 3Fe_2O_3$	−249,450	140.7
$Fe + \frac{1}{2}S_2 = FeS$	−150,247	52.6
$3Fe + C = Fe_3C$	29,037	−28.0
$Co + \frac{1}{2}O_2 = CoO$	−233,886	70.7
$3CoO + \frac{1}{2}O_2 = Co_3O_4$	−183,260	148.1
$Ni + \frac{1}{2}O_2 = NiO$	−234,345	84.3
$H_2 + \frac{1}{2}O_2 = H_2O$	−246,440	54.8
$H_2 + \frac{1}{2}S_2 = H_2S$	−180,580	98.8
$O_2 + \frac{1}{2}S_2 = SO_2$	−362,420	72.4
$CO + \frac{1}{2}O_2 = CO_2$	−282,420	86.8
$2CO = CO_2 + C$	−170,700	174.5

[a]*Referred to pure solid metals (except liquid Al), compounds and graphite. ΔG° values for the mole numbers shown in the chemical equations.*

Thus

$$K_p^2 = \frac{p_{CO}^2 p_{O_2}}{p_{CO_2}^2}$$

$$= \frac{(b+x)^2 \frac{x}{2}}{(a-x)^2} \frac{p}{(a+b+x/2)} \qquad [2.25]$$

Whilst this cubic equation can be solved numerically, use can be made of the fact that x will be small, as is now seen.

For reaction [2.15]

$$\Delta G^\circ = 282,420 - 86.28\ T \text{ J mol}^{-1}$$

and at 1000°C, $\Delta G^\circ_{1273} = 172,586$ J mol^{-1}, and therefore

$$K_p = 8.3 \times 10^{-8}$$

If the input gas contains $n_{CO} = 0.1$, $n_{CO_2} = 0.9$ then clearly x must be very small. Using the approximation $b >> x << a$ in Eq. [2.25] leads to

$$K_p^2 = 6.8 \times 10^{-15} = \left(\frac{0.1}{0.9}\right)^2 \frac{x}{2} p$$

and if $p = 1$ atm, we find $x = 1.1 \times 10^{-12}$, justifying the approximation. The value of p_{O_2} is then given by

$$p_{O_2} = \frac{x/2}{(a+b+x/2)} = 5 \times 10^{-13} \text{ atm}$$

It is seen that the substoichiometric combustion considered in Section 1.1 can lead to quite low oxygen partial pressures. However, to attach significance to this value, it is necessary to consider the thermodynamics of steel oxidation.

2.2 CHEMICAL EQUILIBRIA BETWEEN SOLIDS AND GASES

We consider metal oxidation reactions such as Eq. [2.1], observe that they are of the general form Eq. [2.17] and note that the condition for equilibrium is therefore given by Eq. [2.20]. It is convenient to state this as

$$\mu_{MO} - \mu_M - \frac{1}{2}\mu^\circ_{O_2} - \frac{1}{2}RT \ln p_{O_2} = 0 \qquad [2.26]$$

where the values of μ_{MO}, μ_M in general depend on pressure, temperature and composition, and these dependencies have been stated explicitly for μ_O. However, if the metal and metal oxide are pure, immiscible solids, then their μ values are independent of system composition.

Furthermore, the chemical potentials of solids are insensitive to pressure according to Eq. [2.10], because their molar volumes are small. Thus μ_M, μ_{MO} depend on temperature only, and Eq. [2.26] can be rewritten as

$$\Delta G^\circ = \mu^\circ_{MO} - \mu^\circ_M - \frac{1}{2}\mu^\circ_{O_2} = \frac{1}{2}RT \ln p_{O_2} \qquad [2.27]$$

or equivalently

$$K_p = \exp(-\Delta G^\circ/RT) = \frac{1}{p_{O_2}^{\frac{1}{2}}} \qquad [2.28]$$

At this precisely defined temperature-dependent value of p_{O_2}, the metal and its oxide coexist at equilibrium. This value is often termed the dissociation pressure and will be denoted here as $p_{O_2}(MO)$.

For wüstite formation

$$Fe + \frac{1}{2}O_2 = FeO \qquad [2.29a]$$

we find from Table 2.1

$$\Delta G^\circ = -264,890 + 65.4\ T\ J\ mol^{-1} \qquad [2.29b]$$

and at 1000°C, $\Delta G^\circ_{1273} = -181,640\ J\ mol^{-1}$, corresponding to

$$K_{2.29} = 2.78 \times 10^7,\ p_{O_2}(FeO) = 1.2 \times 10^{-15}\ atm.$$

The symbol K_i will be used to denote the equilibrium constant at fixed total pressure for reaction i. For $p_{O_2} = 1.2 \times 10^{-15}$ atm, iron and wüstite coexist. At lower oxygen partial pressures, a clean iron surface would not oxidise, and any FeO would be reduced to metal. At higher values of p_{O_2}, iron would oxidise, a process which would continue until either the iron was consumed or, if the gas supply was limited, until enough oxygen was consumed to lower p_{O_2} to 1.2×10^{-15} atm.

In the steel reheat furnace considered in Chapter 1, the steel can be regarded in a chemical sense as almost pure iron, and reaction Eq. [2.29a] describes its oxidation. Because fuel is continuously combusted, the ambient p_{O_2} is maintained at a constant value. Even under the strongly substoichiometric combustion conditions leading to a 90/10 mixture of CO_2/CO, this value exceeds the Fe/FeO equilibrium value. Since the steel sections are much larger than can be consumed in the time available, reaction [2.29] continues, forming more scale.

In fact, iron can form two higher oxides

$$3FeO + \frac{1}{2}O_2 = Fe_3O_4,\quad \Delta G^\circ = -312,210 + 125.1\ T\ J\ mol^{-1} \qquad [2.30]$$

$$2Fe_3O_4 + \frac{1}{2}O_2 = 3Fe_2O_3, \Delta G^\circ = -249,450 + 140.7\ T\ J\ mol^{-1} \qquad [2.31]$$

from which we calculate for $T = 1000°C$

$$p_{O_2}(Fe_3O_4) = 2.8 \times 10^{-13} \text{ atm}$$

$$p_{O_2}(Fe_2O_3) = 1.7 \times 10^{-6} \text{ atm}$$

Thus the supposed gas mixture of 10% CO, 90% CO_2 will form magnetite (Fe_3O_4), but not hematite. The question as to how wüstite and magnetite are disposed within the scale is dealt with in the next section.

Standard free energy data for metal oxidation reactions

$$\frac{2x}{y}M + O_2 = \frac{2}{y}M_xO_y \qquad [2.32]$$

are conveniently summarised in Ellingham/Richardson diagrams such as the one shown in Fig. 2.1. Here ΔG° is plotted as the y-axis and temperature as the x-axis. Because all reactions are normalised to 1 mol of O_2, it follows that $\Delta G^\circ = RT \ln p_{O_2}$ and an auxiliary scale in p_{O_2} is possible. The equilibrium value of p_{O_2} for a particular metal-oxide couple is found by drawing a straight line (the dashed line in Fig. 2.1) from the point marked 'O' (at $\Delta G^\circ = 0$, $T = 0K$) through the free energy line of interest at the desired temperature, and continuing the line to its intersection with the p_{O_2} scale on the right hand side of the diagram. Following this procedure for Fe/FeO at 1000°C yields the estimate $p_{O_2} \approx 10^{-15}$ atm, in agreement with the earlier calculation. The justification for this procedure is seen in the equation for the straight line

$$y = a + bx$$

in this case

$$\Delta G^\circ = \frac{\Delta G^\circ_{T_1}}{T_1} T$$

where $T_1 = 1273K$, and $\Delta G^\circ_{T_1}/T_1 = R \ln p_{O_2}(T_1)$. The auxiliary p_{O_2} scale is seen in the diagram to be located at $T_2 \approx 2873K$. Thus the intersection of the dashed line with the p_{O_2} scale is at $\Delta G^\circ = RT_2 \ln p_{O_2}(T_1)$.

Additional scales are provided for the CO/CO_2 and H_2/H_2O ratios corresponding to oxidation equilibria. We consider the example of wüstite formation again. A straight line is drawn from the point marked 'C' on the left (at $\Delta G^\circ = \Delta G^\circ[2.15]$, $T = 0K$) to the Fe/FeO line at 1000°C and continued to the CO/CO_2 scale on the right hand side, yielding an estimate $p_{CO}/p_{CO_2} > 1$. Thus the diagram is useful for obtaining close order of magnitude estimates. Similar diagrams are available for sulphides [4] and carbides [5].

It is seen that the free energy plots in Fig. 2.1 are almost straight lines. Furthermore, most of the lines are approximately parallel, apart from changes in slope corresponding to changes of state. Rewriting Eq. [2.2] as

$$\Delta G^\circ = \Delta H^\circ - T\Delta S^\circ \qquad [2.33]$$

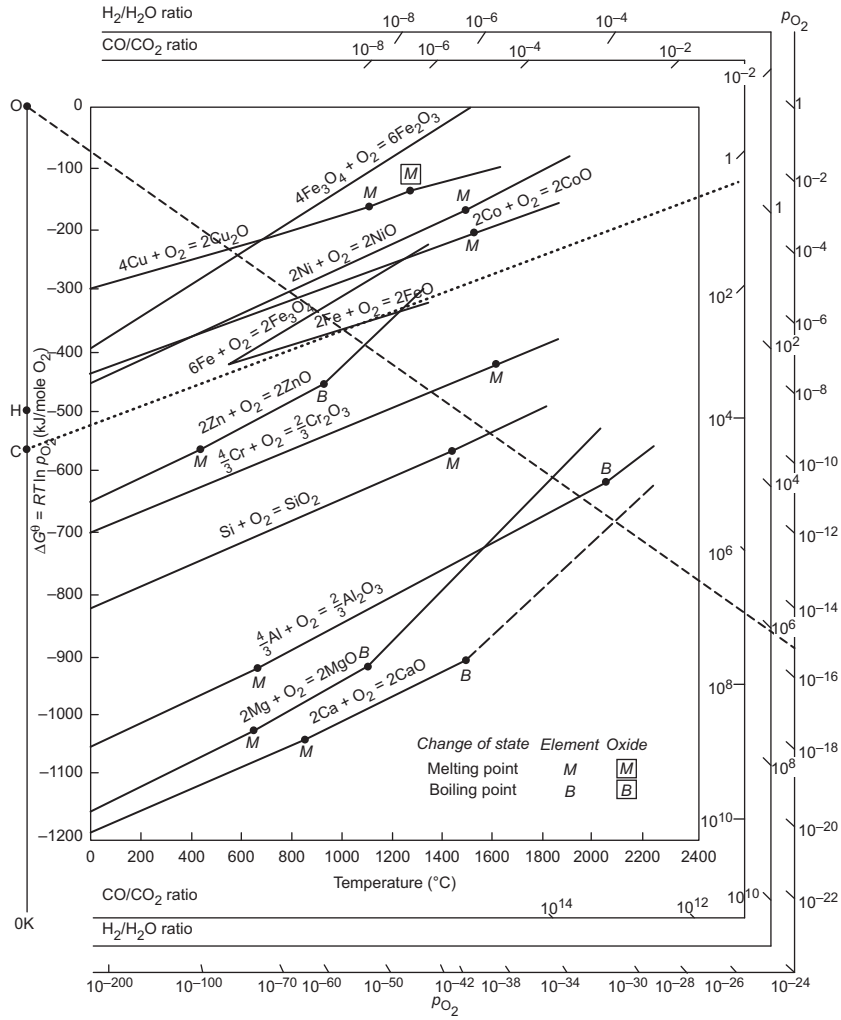

FIGURE 2.1 Ellingham/Richardson diagram showing free energies of formation for selected oxides as a function of temperature, together with corresponding equilibrium p_{O_2} and H_2/H_2O and CO/CO_2 ratios. *Dashed line* to find equilibrium p_{O_2} for Fe/FeO and dotted line to find p_{CO}/p_{CO_2} for same reaction.

it is deduced from the near linearity of the plots that ΔH° and ΔS° are almost constant. It is also seen that the positive slopes of the lines correspond to negative entropy changes. This is a consequence of the fact that the entropy of a gas is much larger than that of a solid. Thus the largest component of ΔS° in reaction [2.32] is associated with the removal of 1 mol from the gas phase. This also explains why the slopes of the lines are approximately equal.

2.2.1 Chemical Equilibria Involving Multiple Solids

In the last section we encountered the situation where the ambient p_{O_2} value was maintained at such a value that two different oxides, FeO and Fe_3O_4, could form: reactions [2.29] and [2.30] were both favoured. Of course, in time, all the iron would be converted to magnetite, which would then equilibrate with the ambient gas. Our interest is in the earlier stages, when the reaction is still in progress, and some iron still remains. In thinking about the structure of the scale, it is useful to consider the metal–scale and scale–gas interfaces. In the latter, reaction [2.30] proceeds to the right at $p_{O_2} > 2.8 \times 10^{-13}$ atm, and we predict that the surface oxide will be magnetite. Consider now what would happen if the underlying metal was in contact with this oxide, by enquiring as to whether the reaction

$$Fe + Fe_3O_4 = 4FeO \qquad [2.34]$$

will proceed. For $T = 1000°C$, we evaluate

$$\Delta G^\circ[2.34] = 4\Delta G^\circ[2.29] - \Delta G^\circ[2.30]$$

$$= -57,360 \text{ J mol}^{-1}$$

and see that wüstite is more stable. It will therefore form between the iron and the magnetite, and a two-layer scale is predicted.

The reasoning above is correct, but tedious. The same conclusion is reached immediately on examining the Fe-O phase diagram in Fig. 2.2. This

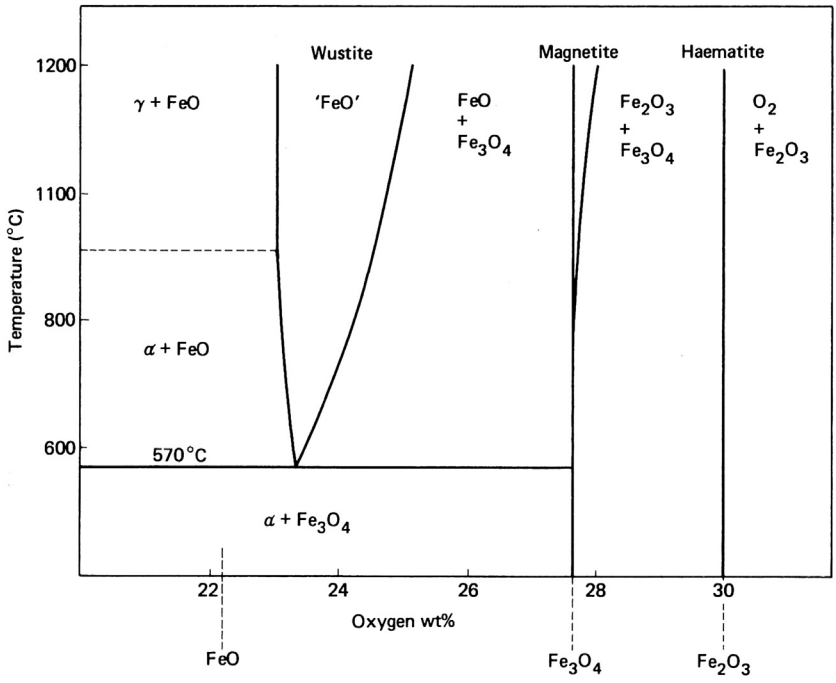

FIGURE 2.2 Iron-oxygen phase diagram.

composition–temperature diagram maps the existence regions of the various possible phases. It is seen that wüstite is not actually 'FeO' but is a metal deficient oxide $Fe_{1-\delta}O$, where δ varies at any given temperature. Magnetite also deviates from its nominal stoichiometry at high temperatures, but the highest oxide, hematite, is closely stoichiometric at all temperatures. The diagram also reveals that wustite is unstable below 570°C.

Phase diagrams summarise experimental observations of equilibrium. The Fe-O diagram informs us that for $1370 > T > 570$°C, iron equilibrates with $Fe_{1-\delta}O$. At high oxygen contents, wustite can coexist with magnetite, magnetite with hematite and hematite with O_2(g). This sequence is the one in which oxide layers are disposed within a scale grown isothermally on iron, as shown in Fig. 2.3. The locus of scale composition across its width, from pure iron to oxygen gas, can be mapped onto the phase diagram, as shown in the figure. The resulting line is termed a 'diffusion path', as it shows the concentration changes which drive diffusion within the reacting system. The significance of the single-phase regions traversed by the diffusion path is clear. However, interpretation of the two-phase regions requires consideration of the phase rule.

Consider a system containing C components (chemical species) and consisting of P phases. In principle, each phase can contain all C components, and its composition is specified by $C-1$ variables. When temperature and pressure are included, the state of each phase is completely specified by $C+1$ variables. For the entire system, we thus find that the total number of variables is $P(C+1)$. At equilibrium, a number of equations are in effect among the variables

$$T_1 = T_2 = \cdots T_p \quad (\mathrm{P}-1 \ \text{ equalities})$$

$$p_1 = p_2 = \cdots p_p \quad (\mathrm{P}-1 \ \text{ equalities})$$

$$\mu_{1,1} = \mu_{1,2} = \cdots \mu_{1,p} \quad (\mathrm{P}-1 \ \text{ equalities for component 1})$$

and a similar set of $(P-1)$ equations for each of the other components. In all, there are $(P-1)\ (C+2)$ equations. It is seen that the number of variables exceeds the number of equations by a number F:

$$F = C - P + 2 \qquad [2.35]$$

This result is the phase rule, and F represents the number of degrees of freedom available to the system. It tells us the number of variables which can be incrementally changed without altering the number of phases present.

Confusion can sometimes arise in determining the number of components, C. The usually stated rule is that C equals the smallest number of constituents whose specification suffices to determine the composition of every phase. Evaluating this number can be a nontrivial exercise in complex chemical systems but is straightforward for alloy oxidation: C equals the number of elements involved. For a binary oxide, $C = 2$. The need to specify both arises from the variable composition of oxide and other solid compounds, as is now demonstrated.

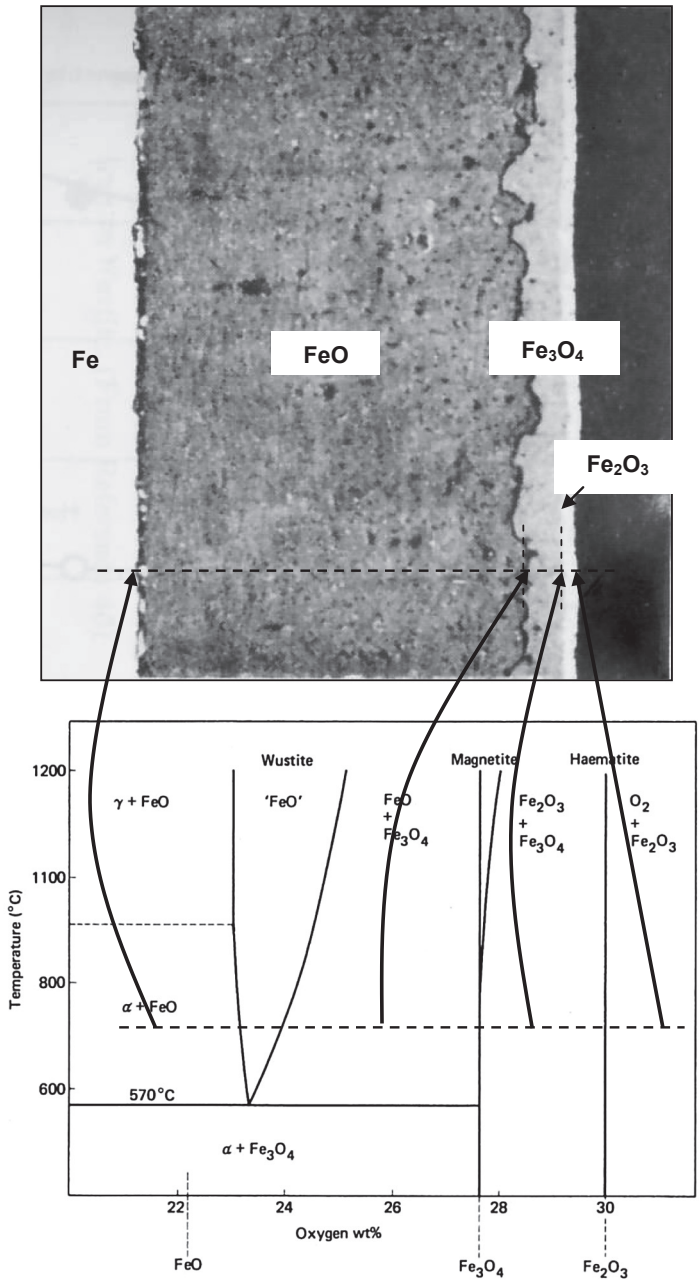

FIGURE 2.3 Cross-section of oxide scale grown on iron, with diffusion path mapped on the phase diagram.

In an isothermal, isobaric situation, such as the oxidation of iron discussed above, the phase rule becomes

$$F = C - P \qquad [2.36]$$

For the two-component Fe-O system, a single-phase region is univariant, ie, its composition can vary. This is self-evidently the case for $Fe_{1-\delta}O$ and Fe_3O_4 at high temperatures. Although it cannot be seen on the diagram, Fe_2O_3 is also capable of very small variations in composition. It is this degree of freedom which permits the development of concentration gradients, which in turn drive the diffusion processes supporting scale growth. In binary two-phase regions, it follows from Eq. [2.36] that $F = 0$, and compositions are fixed. In the absence of any concentration gradient, dispersed two-phase regions cannot grow and are not found in the scale. Instead, two-phase regions consist of sharp interfaces, as seen in Fig. 2.3. For the same reason, wüstite cannot form as particles within the iron. When pure metals are oxidised isothermally, they always grow external scales rather than forming internal oxide precipitates.

2.2.2 Gases Containing Two Reactants

Gases containing two or more oxidants are commonly encountered at high temperatures. For example, most fossil fuels contain sulphur, and combustion leads to the formation of SO_2 and other gaseous species. If iron is exposed to such a gas, then the possible reactions include

$$\mathrm{Fe} + \frac{1}{2}\mathrm{S_2} = \mathrm{FeS} \quad \mathrm{K}_{2.37} = \frac{1}{p_{\mathrm{S_2}}} \qquad [2.37]$$

$$\mathrm{FeO} + \frac{1}{2}\mathrm{S_2} = \mathrm{FeS} + \frac{1}{2}\mathrm{O_2} \quad \mathrm{K}_{2.38} = \frac{p_{\mathrm{O_2}}^{\frac{1}{2}}}{p_{\mathrm{S_2}}^{\frac{1}{2}}} \qquad [2.38]$$

$$\mathrm{Fe_3O_4} + \frac{3}{2}\mathrm{S_2} = 3\mathrm{FeS} + 2\mathrm{O_2} \quad K_{2.39} = \frac{p_{\mathrm{O_2}}^{2}}{p_{\mathrm{S_2}}^{\frac{3}{2}}} \qquad [2.39]$$

$$\mathrm{Fe_2O_3} + \mathrm{S_2} = 2\mathrm{FeS} + \frac{3}{2}\mathrm{O_2} \quad K_{2.40} = \frac{p_{\mathrm{O_2}}^{\frac{3}{2}}}{p_{\mathrm{S_2}}} \qquad [2.40]$$

as well as reactions producing sulphates, which will be ignored here for the sake of simplicity. The gas phase reactions of importance are

$$\mathrm{SO_2} = \frac{1}{2}\mathrm{S_2} + \mathrm{O_2}, \quad K_{2.41} = \frac{p_{\mathrm{S_2}}^{\frac{1}{2}} p_{\mathrm{O_2}}}{p_{\mathrm{SO_2}}} \qquad [2.41]$$

and, at high oxygen partial pressures,

$$\mathrm{SO_2} + \frac{1}{2}\mathrm{O_2} = \mathrm{SO_3}, \quad K_{2.42} = \frac{p_{\mathrm{SO_3}}}{p_{\mathrm{SO_2}} p_{\mathrm{O_2}}^{\frac{1}{2}}} \qquad [2.42]$$

The ternary system Fe-S-O can be analysed thermodynamically in the same way as was done for the Fe-O system, but the multiple equilibria make the process complex. As seen from the phase rule, up to three phases can coexist at interfaces, and two-phase scale layers can grow.

Interpretation of this situation is much easier using a phase diagram, such as the one drawn in Fig. 2.4 on the assumption that all solids are pure and immiscible. Logarithmic scales are used for p_{S_2} and p_{O_2} in order to encompass the large ranges involved and have the advantage of linearising the equilibrium relationships of Eqs [2.37]−[2.40]. Thus, for example, the phase boundary between FeO and FeS is defined as a straight line by the equation

$$\log p_{O_2} = \log p_{S_2} + 2 \log K_{2.38} \qquad [2.43]$$

and has a slope equal to one.

The diagram unambiguously defines the range of gas compositions in which pure iron is stable as a metal ($p_{O_2} < 1 \times 10^{-19}$ atm and $p_{S_2} < 7 \times 10^{-10}$ atm at $T = 800°C$). It also allows prediction of which of the possible reaction products can coexist with an equilibrium gas mixture. Thus, for example, at $p_{S_2} = 1 \times 10^{-7}$ atm and $p_{O_2} = 1 \times 10^{-14}$ atm, the surface of a scale is expected to be magnetite (point *A*). However, it is not possible to predict the diffusion path trajectory, from *A* to *B*, from thermodynamic information alone. Three possibilities are shown in Fig. 2.4, one involving oxide, but the other two also involving sulphide. Since sulphides generally grow much faster than oxides, the question is important and is considered further in Chapters 4 and 8.

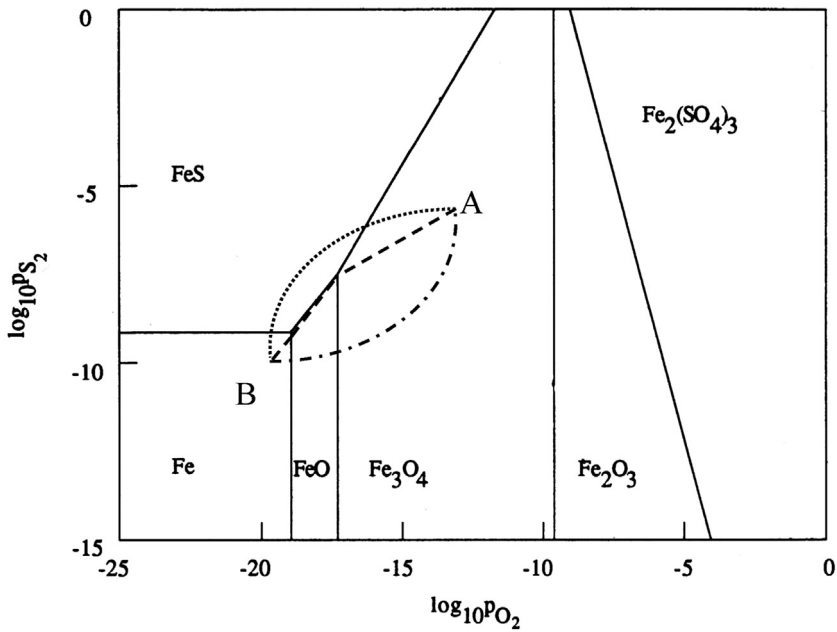

FIGURE 2.4 Thermochemical (Kellogg) diagram for Fe-S-O system at 800°C, showing three possible diffusion paths for reaction with Gas A.

2.3 ALLOYS AND SOLID SOLUTIONS

Alloy phases are in general solid solutions, and the need arises to specify component activities within them. Returning to Eq. [2.3], we note that the changes in composition, dn_i, now to be considered reflect alteration of solute concentration rather than chemical reaction. Taking the total differential of Eq. [2.8]

$$dG = \sum_i \mu_i dn_i + \sum_i n_i d\mu_i \qquad [2.44]$$

and subtracting it from Eq. [2.5], we obtain the Gibbs–Duhem equation

$$0 = Vdp - SdT - \sum_i n_i d\mu_i \qquad [2.45]$$

Again, summations are performed over all components of the system. We consider an isothermal, isobaric system in which, at equilibrium,

$$\sum_i n_i d\mu_i = 0 \qquad [2.46]$$

or, dividing by the total number of component moles, n_T, to obtain mole fractions

$$\sum N_i d\mu_i = 0 \qquad [2.47]$$

Consistent with the approach adopted for ideal gas mixtures (Eq. [2.14]), the solution component activity is defined through

$$\mu_i - \mu_i^\circ = RT \ln a_i = \overline{G}_i - \overline{G}_i^\circ \qquad [2.48]$$

where unit activity corresponds to the standard state in which $\mu_i = \mu_i^\circ$. The choice of standard state is arbitrary, but that of pure solid is convenient. In this case, an ideal solution is defined as one in which the chemical potential of every component is related to its mole fraction by

$$\mu_i - \mu_i^\circ = RT \ln N_i \qquad [2.49]$$

Real solutions deviate from ideality and are dealt with by defining an activity coefficient, γ_i, such that the relationship

$$\mu_i - \mu_i^\circ = RT \ln \gamma_i N_i \qquad [2.50]$$

holds, whatever the extent of deviation. In general, γ_i varies with composition, as well as with temperature and pressure.

The thermodynamics of solutions can be understood from their enthalpy and entropy of mixing. At a constant pressure, the application of Eqs [2.2]

and [2.48] to a particular component in a solution of fixed composition yields

$$\frac{\partial\left(\overline{G}_i/T\right)}{\partial(1/T)} = \overline{H}_i \qquad [2.51]$$

and hence

$$\frac{\partial\left(\frac{\mu_i - \mu_i^\circ}{T}\right)}{\partial(1/T)} = \overline{H}_i - H_i^\circ \qquad [2.52]$$

where H_i° is the standard enthalpy per mole of unmixed component i, and overscoring indicates the partial molar quantity. Comparison with Eq. [2.48] then leads to

$$R\frac{\partial \ln a_i}{\partial(1/T)} = \overline{H}_i - H_i^\circ \qquad [2.53]$$

For an ideal solution, $a_i = N_i$, and the partial differential in Eq. [2.49] is zero, the enthalpy of the dissolved component being equal to its value in the unmixed state. The enthalpy of mixing is defined for the entire solution as

$$\Delta H_m = \sum_i N_i \overline{H}_i - \sum_i N_i H_i^\circ \qquad [2.54]$$

and in the ideal case, $\Delta H_m^{\text{id}} = 0$.

If Eq. [2.48] is multiplied by N_i and a sum formed for all components, we obtain

$$\sum_i N_i \overline{G}_i - \sum_i N_i G_i^\circ = RT \sum N_i \ln a_i \qquad [2.55]$$

in which the left-hand side is recognised as the free energy of mixing

$$\Delta G_m = G - \sum_i N_i G_i^\circ \qquad [2.56]$$

In an ideal solution, therefore,

$$\Delta G_m^{\text{id}} = RT \sum N_i \ln N_i \qquad [2.57]$$

and it follows from the equation

$$\left(\frac{\partial \Delta G}{\partial T}\right)_{P,n_i} = -\Delta S \qquad [2.58]$$

that

$$\Delta S_m^{\text{id}} = -R \sum N_i \ln N_i \qquad [2.59]$$

This expression is recognised from the Boltzmann equation,

$$S = k \ln \omega$$

where ω is a measure of randomness and k is Bolzmann's constant, as corresponding to a random mixture. This is now illustrated for a binary mixture of A and B

$$\begin{aligned} \Delta S_m^{\text{id}} &= S_{\text{mix}} - S_A - S_B \\ &= k \ln \left(\frac{(n_A + n_B)!}{n_A! n_B!} \right) \end{aligned} \quad [2.60]$$

where n_i is the number of atoms of the indicated species, and ω has been evaluated as the number of distinguishable configurations of the $n_A + n_B$ atoms. Expanding Eq. [2.60] with the aid of Stirling's approximation

$$\ln n! = n \ln n - n \quad [2.61]$$

and the relationship $R = kN_{\text{AV}}$ (with N_{AV} equal to Avogrado's number) leads to

$$\Delta S_m^{\text{id}} = -R(N_A \ln N_A + N_B \ln N_B) \quad [2.62]$$

which is merely Eq. [2.59] applied to a binary system. Thus an ideal solution is a completely random mixture of constituents which experience the same thermal interaction with all neighbouring atoms, and the entropy of mixing is purely configurational.

In real solutions, interactions between dissimilar atoms give rise to non-zero $\overline{H}_i$ and thermal contributions to $\overline{S}_i$. These are conveniently described using 'excess' functions of the sort

$$G^{\times s} = G - G^{\text{id}} \quad [2.63]$$

Rewriting Eq. [2.48] as

$$RT \ln \gamma_i = \overline{G}_i - G_i^{\circ} - RT \ln N_i \quad [2.64]$$

and substituting for $RT \ln N_i$ from Eq. [2.49] we find

$$\begin{aligned} RT \ln \gamma_i &= \left(\overline{G}_i - G_i^{\circ}\right) - \left(\overline{G}_i^{\text{id}} - G_i^{\circ}\right) \\ &= \overline{G}_i - G_i^{\text{id}} \\ &= \overline{G}_i^{\times s} = \overline{H}_i^{\times s} - T\overline{S}^{\times s} \end{aligned} \quad [2.65]$$

Since $\overline{H}_i^{\text{id}} = 0$, this is equivalent to

$$RT \ln \gamma_i = \overline{H}_i - T\overline{S}^{\times s} \quad [2.66]$$

where the deviation from ideality of component i is seen to arise from its thermal interaction with the solution and the consequent shift in thermal entropy. A useful tabulation of partial molar excess quantities $\overline{G}^{\times s}$, $\overline{H}^{\times s}$ and $\overline{S}^{\times s}$ has been provided by Kubaschewski et al. [1] for binary alloy systems.

An alternative approach is suited to dilute solutions where the experimental finding is that

$$a_i = \gamma_i^{\circ} N_i \qquad [2.67]$$

with γ_i° a constant. This is Henry's law. More generally, the quantity γ_i varies with composition and can be expanded, as proposed by Wagner [6], as a Taylor series which to the first order yields

$$\ln \gamma_i = \ln \gamma_i^{\circ} + \sum \varepsilon_{ik} N_k \qquad [2.68]$$

where the ε_{ij} are interaction coefficients. It can be shown that

$$\frac{\partial \ln \gamma_i}{\partial N_k} = \varepsilon_{ik} = \varepsilon_{ki} = \frac{\partial \ln \gamma_k}{\partial N_i} \qquad [2.69]$$

lessening the amount of experimentation needed. Although there are many alternative solution models available, the form Eq. [2.68] is a useful one for moderately dilute solutions.

2.3.1 Dissolution of Gases in Metals

In studying the formation of internally precipitated oxides, carbide, etc. (see Fig. 1.8), it is necessary to consider the dissolution of the oxidant in the metal, eg,

$$\frac{1}{2}\mathrm{O_2(g)} = \underline{\mathrm{O}} \qquad [2.70]$$

Here, and elsewhere in this book, underscoring is used to denote a solute species in a solid. It is convenient to specify concentrations as mole fractions, N_i, and we write

$$N_{\mathrm{O}} = K_{70} p_{\mathrm{O_2}}^{\frac{1}{2}} \qquad [2.71]$$

which is Sievert's equation. It was the experimental demonstration of Eq. [2.71] that proved that gaseous oxygen, nitrogen and sulphur dissolve in metals as dissociated atoms. The value of K_{70} is related to that of ΔG° for Eq. [2.70] in the usual way, but care is needed in specifying the concentration units and standard state for the solute. In much of the published work, concentration is expressed in wt%, and a standard state of one wt% is chosen. It is preferable to use a mole fraction, N_{O}, so that

$$\Delta G[2.70] = \Delta \overline{H} - T\Delta \overline{S}^{\times s} + RT \ln N_{\mathrm{O}} - \frac{1}{2} RT \ln p_{\mathrm{O_2}} \qquad [2.72]$$

Data for oxygen solubility in iron and nickel are summarised in Table 2.2, and corresponding data for carbon are provided in Table 9.4.

The maximum value of $p_{\mathrm{O_2}}$ applicable in Eq. [2.71] is the equilibrium value for the formation of the lowest metal oxide. Thus, for example, the maximum solubility of oxygen in austenitic iron is set by the Fe/FeO equilibrium. As seen earlier, at $T = 1000^{\circ}\mathrm{C}$, $p_{\mathrm{O_2}}(\mathrm{FeO}) = 1.2 \times 10^{-15}$ atm. Calculating K_{70} from the data in Table 2.2, this is found to correspond to a

TABLE 2.2 Oxygen Dissolution in Metals[a]

Metal	$\Delta\bar{H}_O$/kJ mol^{-1}	$\Delta\bar{S}_O^{\times s}$/J mol^{-1} K^{-1}	References[b]
Ni	−182	−107.6	[A6]
α-Fe	−155.6	−81.0	[A9]
γ-Fe	−175.1	−98.8	[A9]

[a]*Referred to Eq. [2.72] with p_{O_2} (atm) and N_O (mole fraction).*
[b]*References in Appendix D.*

solubility limit of 3.7×10^{-6} mol fraction in the iron beneath an oxide scale. In the case of an alloy, if sufficient dissolved oxygen is present, it can react with an alloy metal solute to precipitate particles of oxide, a situation considered in the next section.

2.4 CHEMICAL EQUILIBRIA BETWEEN ALLOYS AND GASES

2.4.1 Equilibria Between Alloys and Single Oxide

Consider a binary alloy A-B reacting with oxygen. In general, $\Delta G^\circ(\text{AO}) \neq \Delta G^\circ(\text{BO})$ and one of the metal oxides is more stable than the other. Referring to Table 1.1, we see that, eg, the alloys Fe-Ni and Fe-Cr are of interest, because the growth of NiO or Cr_2O_3 is much slower than that of FeO. We enquire as to the alloy concentration of nickel or chromium necessary to form the desired oxide. This situation can be formulated as a competitive oxidation reaction, eg,

$$\underline{\text{Ni}} + \text{FeO} = \text{NiO} + \underline{\text{Fe}} \qquad [2.73]$$

The condition for chemical equilibrium, $\sum \nu_i \mu_i = 0$, after substitution from Eq. [2.48] yields

$$\Delta G^\circ = \mu^\circ_{\text{Fe}} + \mu^\circ_{\text{NiO}} - \mu^\circ_{\text{Ni}} - \mu^\circ_{\text{FeO}} = -RT \ln \frac{a_{\text{NiO}} a_{\text{Fe}}}{a_{\text{FeO}} a_{\text{Ni}}} \qquad [2.74]$$

For simplicity, we approximate the oxides as being pure, immiscible solids, so that $a_{\text{NiO}} = 1 = a_{\text{FeO}}$. The standard free energy change is evaluated from

$$\Delta G^\circ[2.73] = \Delta G^\circ(\text{NiO}) - \Delta G^\circ(\text{FeO}) \qquad [2.75]$$

as +55,760 J mol^{-1} at 1000°C. Thus, at equilibrium,

$$\frac{a_{\text{Ni}}}{a_{\text{Fe}}} = 194 \qquad [2.76]$$

and the alloy needs a very high nickel content. Approximating the alloy as an ideal solution and rewriting Eq. [2.76] as

$$\frac{N_{\text{Ni}}}{1 - N_{\text{Ni}}} = 194 \qquad [2.77]$$

we find the solution $N_{\text{Ni}} = 0.995$. It is clear that alloying with nickel cannot be used as a method of achieving oxidation resistance for a steel.

Turning now to the Fe-Cr alloy, we formulate the competitive reaction

$$2\underline{\mathrm{Cr}} + 3\mathrm{FeO} = \mathrm{Cr_2O_3} + 3\underline{\mathrm{Fe}} \qquad [2.78]$$

for which the equilibrium expression is

$$\frac{a_{\mathrm{Cr_2O_3}} a_{\mathrm{Fe}}^3}{a_{\mathrm{FeO}}^3 a_{\mathrm{Cr}}^2} = \exp[-\Delta G^\circ[2.78]/RT] \qquad [2.79]$$

Pure, immiscible oxides are again assumed so that their activities can be set to unity, and the standard free energy change is evaluated from

$$\Delta G^\circ[2.78] = \Delta G^\circ(\mathrm{Cr_2O_3}) - 3\Delta G^\circ(\mathrm{FeO}) \qquad [2.80]$$

as $-244{,}590\ \mathrm{J\ mol^{-1}}$ at 1000°C, corresponding to

$$\frac{a_{\mathrm{Cr}}^2}{a_{\mathrm{Fe}}^3} = 9 \times 10^{-11} \qquad [2.81]$$

Assuming that in such a dilute solution $a_{\mathrm{Fe}} = N_{\mathrm{Fe}} \approx 1$, it is found that $a_{\mathrm{Cr}} \approx 1 \times 10^{-5}$. Data tabulated by Kubaschewski et al. [1] for ferritic Fe-Cr alloys show that for $N_{\mathrm{Cr}} \to \mathrm{O}$, $\Delta\overline{H}_{\mathrm{Cr}} = +25{,}100\ \mathrm{J\ mol^{-1}}$ and $\Delta\overline{S}_{\mathrm{Cr}}^{\times s} = +10.25\ \mathrm{J\ mol^{-1} K^{-1}}$. Insertion of these values in Eq. [2.66] yields the value $\gamma_{\mathrm{Cr}} = 3.1$ at 1000°C. Thus the required chromium activity of 1×10^{-5} is equivalent to $N_{\mathrm{Cr}} \approx 3 \times 10^{-6}$. Thermodynamically, at least, the use of chromium as a steel alloying addition for oxidation protection is seen to be very attractive.

The question as to whether the oxide forms as an external scale or as internal precipitates requires kinetic analysis. Assuming for the moment that internal oxidation occurs within a dilute alloy, it is seen that the reaction is one between solute species

$$2\underline{\mathrm{Cr}} + 3\underline{\mathrm{O}} = \mathrm{Cr_2O_3} \qquad [2.82]$$

The value of $\Delta G[2.82]$ is found from the reactions

$$2\mathrm{Cr} + \frac{3}{2}\mathrm{O_2(g)} = \mathrm{Cr_2O_3} \qquad [2.83]$$

$$\mathrm{Cr} = \underline{\mathrm{Cr}} \qquad [2.84]$$

$$\frac{1}{2}\mathrm{O_2} = \underline{\mathrm{O}} \qquad [2.85]$$

for which we can write

$$\Delta G^\circ[2.83] = -1{,}120{,}270 + 259.83\ \mathrm{T\ J\ mol^{-1}} \qquad [2.86]$$

$$\Delta\overline{G}_{\mathrm{Cr}}[2.84] = 25{,}100 - 10.25\ \mathrm{T} + RT \ln N_{\mathrm{Cr}}\ \mathrm{J\ mol^{-1}} \qquad [2.87]$$

$$\Delta\overline{G}_o[2.85] = -175,100 + 98.8\ \mathrm{T} + RT\ln N_\mathrm{O}\ \mathrm{J\ mol^{-1}} \qquad [2.88]$$

where Eq. [2.72] has been used to find Eq. [2.87], and Eq. [2.88] was calculated using data for γ-Fe provided by Kubaschewski et al. [1]. From

$$\Delta G[2.82] = \Delta G^\circ[2.83] - 2\Delta\overline{G}_\mathrm{Cr}[2.84] - 3\Delta\overline{G_\mathrm{O}}[2.85]$$

we find, at equilibrium,

$$0 = \Delta G[2.82] = -645,170 - 16.07\ \mathrm{T} - 2RT\ln N_\mathrm{Cr} - 3RT\ln N_\mathrm{O} \qquad [2.89]$$

and at $T = 1000°\mathrm{C}$,

$$N_\mathrm{Cr}^2 N_\mathrm{O}^3 = K_\mathrm{sp} = 4 \times 10^{-28} \qquad [2.90]$$

The equilibrium constant, K_sp, is known as the solubility product.

The maximum value of p_{O_2} available to a dilute Fe-Cr alloy is the level set by the Fe-FeO equilibrium, because a scale forms on the alloy surface. As seen earlier, this value is 1.2×10^{-15} atm for pure iron at 1000°C, and results in $N_\mathrm{O} = 3.1 \times 10^{-6}$. It follows from Eq. [2.90] that the precipitation of Cr_2O_3 within the alloy would leave an equilibrium value $N_\mathrm{Cr} = 2.8 \times 10^{-5}$. It is therefore concluded that any Fe-Cr alloy containing more than 28 ppm of chromium can form internal Cr_2O_3 precipitates when oxidised at 1000°C. Whether or not an external Cr_2O_3 scale forms cannot be predicted from thermodynamics alone.

The preceding discussion of Fe-Ni and Fe-Cr alloy oxidation has been based on the simplifying assumption that the product oxides are pure, immiscible solids. This assumption is not always valid. The Fe-Ni-O system forms a solid solution spinel phase $Ni_xFe_{3-x}O_4$, and the Fe-Cr-O system develops several mixed oxides. These complications are best described with the help of phase diagrams.

2.4.2 Equilibria Between Alloys and Multiple Oxides

A binary alloy reacting with a single oxidant constitutes a ternary system. The phase assemblages capable of coexisting at local equilibrium at a fixed temperature can be represented by an isothermal section of the phase diagram. An example for Fe-Cr-O shown in Fig. 2.5, is drawn as a Gibbs composition triangle. The geometry of the equilateral triangle is such that for any point within the triangle, wherever located, the sum of the perpendiculars to the three sides is always the same. This provides a convenient means of mapping compositions where $N_\mathrm{Fe} + N_\mathrm{Cr} + N_\mathrm{O} = 1$, avoiding the need to calculate the third component which would arise if normal rectangular coordinates were used.

Single phase existence regions are marked on the diagram. The two alloy phases are shown on the Fe-Cr binary side of the triangle: austenite, containing

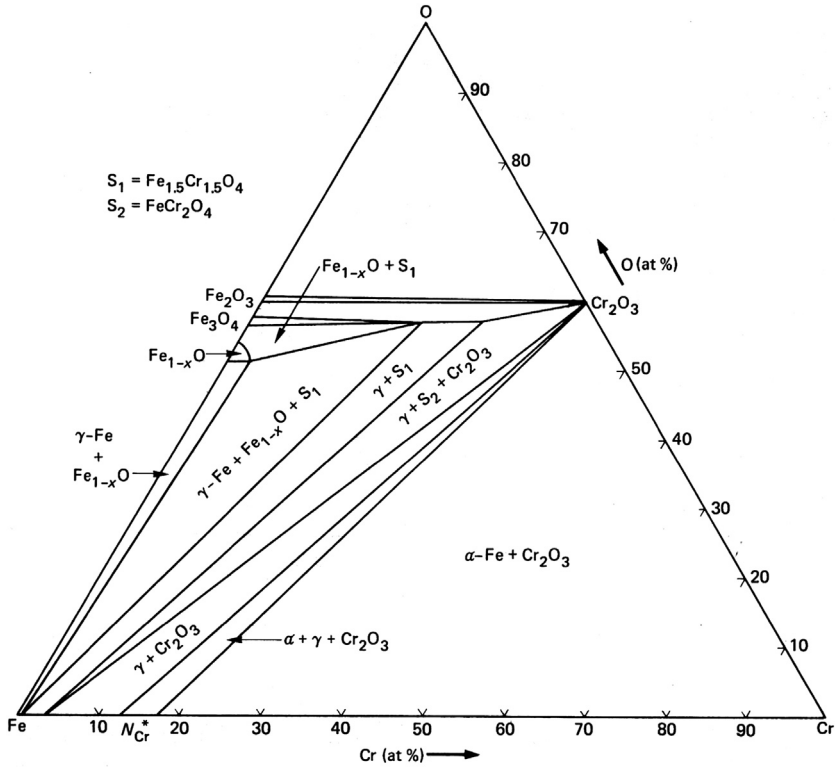

FIGURE 2.5 Isothermal section (1200°C) of Fe-Cr-O phase diagram, with alloy phases omitted for clarity.

$N_{Cr} \leq 0.13$, and ferrite, with $N_{Cr} \geq 0.17$. The three iron oxides are shown along the Fe-O binary side and the single chromium oxide on the Cr-O side.

It is seen that $Fe_{1-\delta}O$ dissolves a significant amount of chromium, the solubility varying with wüstite stoichiometry. The spinel phase Fe_3O_4 dissolves large amounts of chromium, up to a terminal composition of $FeCr_2O_4$. Finally, the structurally isotypic Fe_2O_3 and Cr_2O_3 form a continuous solid solution at this temperature.

As the phase rule informs us, there are two degrees of freedom within a ternary single-phase region, as is illustrated by the representation on the diagram of single phases as areas. When two phases coexist, only one degree of freedom is available. Two-phase regions separate pairs of adjacent single phases, as shown more clearly in the enlarged schematic diagram of Fig. 2.6. Each two-phase region is defined by a set of tie lines, which join pairs of composition points along the phase boundaries. Thus, for example, compositions of wüstite along the line *ab* equilibrate with spinel compositions along the line *cd*.

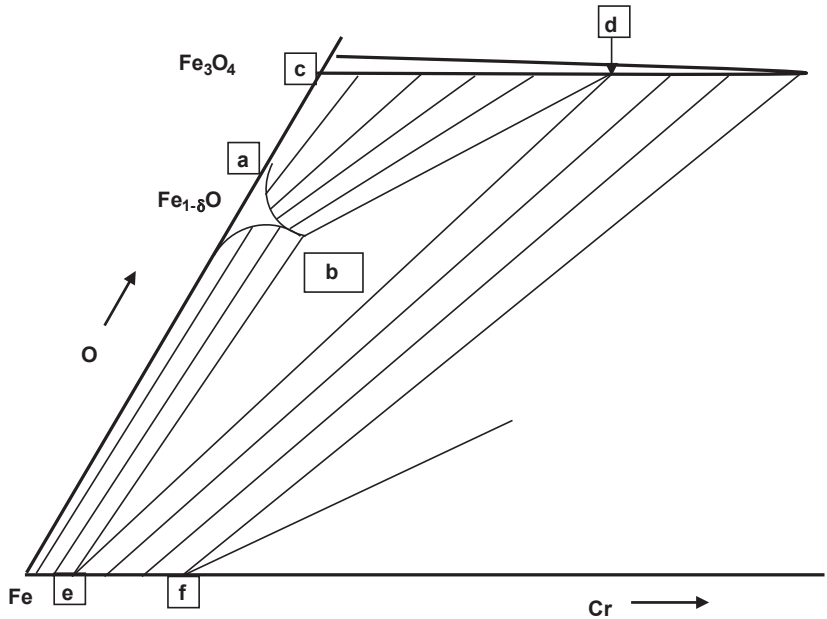

FIGURE 2.6 Schematic enlargement of part of Fig. 2.5.

For all points on any one tie line

$$\mu_{Fe}(W) = \mu_{Fe}(Sp)$$
$$\mu_{Cr}(W) = \mu_{Cr}(Sp)$$
$$\mu_{O}(W) = \mu_{O}(Sp)$$

where W denotes wüstite and Sp the spinel. Of course, different tie lines correspond to different compositions of the phases, and therefore different chemical potentials. The two-phase region is univariant, and this is represented by the lines *ab* and *cd*, which define the composition of each phase in terms of a single variable.

The two-phase regions bound three-phase triangles, eg, the wustite-spinel-alloy triangle *bde*, which represent invariants. All points within the triangle correspond to differing proportions of these three phases, always of the compositions given by the points *b*, *d* and *e*. Thus the relationships $\mu_{Fe}(W) = \mu_{Fe}(Sp) = \mu_{Fe}(Alloy)$, etc. are satisfied.

As we have already seen when examining Fig. 2.4, ternary phase diagrams have some utility in predicting the outcome of alloy oxidation reactions, but diffusion paths cannot be predicted without additional information. The Fe-Cr-O diagram reveals that a necessary condition for the formation of Cr_2O_3 at the scale−metal interface is a surface alloy chromium concentration

greater than that at the point *f*, ie, $N_{Cr} \geq 0.04$. This is much higher than the value calculated from Eq. [2.79] as $a_{Cr} \approx 10^{-4}$ at 1200°C. The difference arises from the neglect of spinel formation in the earlier treatment. As the Fe-Cr-O diagram shows, chromium-rich spinel has a stability equal to that of Cr_2O_3 when $N_{Cr} \approx 0.04$ at 1200°C.

The competitive oxidation reaction is reformulated as

$$\underline{Fe} + \frac{4}{3}Cr_2O_3 = FeCr_2O_4 + \frac{2}{3}\underline{Cr} \qquad [2.91]$$

for which

$$\Delta G^\circ[2.91] = 56,690 - 14.0\,T \text{ J mol}^{-1}$$

and

$$K = \frac{a_{FeCr_2O_4} a_{Cr}^{\frac{2}{3}}}{a_{Cr_2O_3}^{\frac{4}{3}} a_{Fe}} \qquad [2.92]$$

Assuming that the oxides are pure and immiscible and approximating $a_{Fe} \approx N_{Fe} \approx 1$, it is found that

$$\Delta G^\circ = -RT \ln K = -\frac{2}{3}\Delta\mu_{Cr} \qquad [2.93]$$

and at 1200°C, $\Delta\mu_{Cr} = -54{,}102$ J mol^{-1}. Using Eq. [2.87], it is then found that the value of N_{Cr} satisfying the equilibrium between spinel and Cr_2O_3 is 0.03, in reasonable agreement with the phase diagram. Clearly the latter provides a simpler route to the answer, when available for the temperature of interest.

The use of the Fe-Cr-O diagram is considered in more detail in Sections 5.3 and 7.3. However, it should be noted that the condition $N_{Cr} > 0.04$ is insufficient to achieve protective Cr_2O_3 scale formation. The main reason for this is depletion of chromium from the alloy surface by its preferential oxidation. The actual surface concentration is determined by the balance between chromium diffusion from the alloy interior and its removal into the scale.

2.5 THERMODYNAMICS OF DIFFUSION

2.5.1 Driving Forces

We start by considering the thermodynamic implications of matter diffusing from one part of a system to another. In an isothermal, field-free system, an amount dn_{A2} of component *A* passes from region 2 to region 1, with each region being regarded as homogeneous. The changes are described using Eq. [2.3] by

$$dU - TdS = -p_1 dV_1 - p_2 dV_2 + (\mu_{A1} - \mu_{A2})dn_{A2} \qquad [2.94]$$

and the last term reflects the fact that $dn_{A1} = -dn_{A2}$. In a slow process, the p_i do not vary, and

$$p_1 dV_1 - p_2 dV_2 = dw \qquad [2.95]$$

the amount of work done on the system. From the second law of thermodynamics, we have

$$d(U - TS) < dw \qquad [2.96]$$

for a spontaneous process. It follows that the necessary condition for isothermal mass transfer to occur is

$$(\mu_{A1} - \mu_{A2}) dn_{A2} < 0 \qquad [2.97]$$

In other words, the sign of dn_{A2} is the opposite of the sign of $(\mu_{A1} - \mu_{A2})$: if dn_{A2} is a positive transfer of component A from region 2 to region 1, the chemical potential in region 2 must be greater than in region 1. This important result informs us that diffusion actually occurs from regions of high to low chemical potential, rather than from high to low concentration. Thus the simple description given by Fick's law for the relationship between flux and concentration gradient

$$J = -D\frac{\partial C}{\partial x} \qquad [1.24]$$

can be inaccurate to the point of predicting diffusion in the wrong direction.

In developing a more accurate description of diffusion, several approaches are possible. These include geometric, random walk procedures which have been applied to crystalline solids to yield an advanced theory of correlation and isotope effects [7,8] and the application of absolute rate theory. Before developing the latter treatment, we consider a phenomenological approach based on irreversible thermodynamics. The principal concepts were developed by Onsager [9] and extended by de Groot [10] and Prigogine [11]. Their application to solid-state diffusion has been reviewed a number of times [8,12,13].

An essential element of the thermodynamic treatment of diffusion is the postulate that a state of local equilibrium can be adequately approximated in each region of the solid, despite the compositional variation with position within the system. The simultaneous satisfaction of these two requirements is achieved by taking a microscopic volume element which is so small that its composition can be treated as homogeneous. Because the solid is atomically dense, the element contains a statistically meaningful number of particles. A series of such elements describes the diffusion profile within the solid (Fig. 3.32).

The procedures of irreversible thermodynamics enable us to calculate the rate of entropy production per unit volume, $\dot{s}$, in terms of the various fluxes flowing within the system. The result is a bilinear expression involving the fluxes themselves and a set of thermodynamic forces, $\mathbf{X_i}$,

$$T\dot{s} = -\sum_i J_i \mathbf{X_i}$$

These forces are thereby identified as those responsible for the fluxes, each flux being linearly dependent on all the forces. The description is applicable only to systems that are not far removed from equilibrium and is therefore appropriate to diffusion in a solid within which the local equilibrium state is closely approached.

For isothermal diffusion in a closed, isobaric and field-free n-component system, it is found that

$$T\dot{s} = -\sum_{i=1}^{n} J_i \nabla \eta_i \qquad [2.98]$$

where ∇ indicates gradient, ie, partial derivative with respect to position coordinate, and the summation covers all components. Hence the component fluxes are given by a set of linear equations

$$J_i = -\sum_{j=1}^{n} L_{ij} \nabla \eta_j \qquad [2.99]$$

where the L_{ij} are the Onsager phenomenological coefficients. These each relate the flux of species i to the gradient in species j and form a square matrix of order equal to the number of system components. The driving forces are seen to be the gradients $\nabla \eta_i$, known as electrochemical potential gradients. They are defined by

$$\eta = \mu + qF\psi \qquad [2.100]$$

where q is the charge of the species, F is the Faraday and ψ the local electrostatic potential. Gradients in potential constitute fields, but these are internal to the solid, and the conditions for the validity of Eq. [2.98] are maintained. In the case of a metallic alloy, the constituent atoms have no effective charge, and the driving force is the chemical potential gradient, $\nabla \mu$. This result is intuitively satisfactory in the sense that diffusion is perceived (under the conditions specified earlier) as a process that eliminates differences in chemical potential, thereby achieving equilibration.

A more profound result of the irreversible thermodynamic treatment is the recognition that the flux of any component is, in general, dependent on the chemical potential gradients of all components. The $L_{ij} (i \neq j)$ in Eq. [2.99] are referred to as off-diagonal coefficients, and represent the 'cross-effects' between components. These cross-effects can arise from thermodynamic interactions (cf Eq. [2.68]) or from kinetic interactions. Aspects of the latter are outlined in Appendix B for ionic solids. For the moment, we consider the situation where cross-effects are small enough to ignore.

For one-dimensional diffusion in a binary alloy, the approximation $L_{12} \approx 0$ yields the simple result

$$J_1 = -L_{11} \frac{\partial \mu_1}{\partial x} \qquad [2.101]$$

which, upon substitution for μ_1 from Eq. [2.50], leads to

$$J_1 = -\frac{L_{11}RT}{\gamma_1 N_1}\left(\frac{\gamma_1 \partial N_1}{\partial x} + N_1\frac{N_1 \partial \gamma_1}{\partial x}\right)$$

$$= -\frac{L_{11}RT}{N_1}\left(1 + \frac{\partial \ln \gamma_1}{\partial \ln N_1}\right)\frac{\partial N_1}{\partial x} \qquad [2.102]$$

Noting that the change in molar concentration $\partial C_1 = C\partial N_1$, with C the average molar concentration, it is found from a comparison of Eq. [1.24] and Eq. [2.102] that

$$D_1 = -\frac{L_{11}RT}{C_1}\left(1 + \frac{\partial \ln \gamma_1}{\partial \ln N_1}\right) \qquad [2.103]$$

This makes clear that chemical diffusion is strongly dependent on the thermodynamic properties of the solid solution, even in the absence of kinetic cross-effects. The shortcoming of the phenomenological description Eq. [2.99] is that it provides no information on the coefficients L_{ij} relating the diffusion rate to the driving forces. For our present purposes, a more transparent description is provided by an absolute rate theory approach. Before developing this description, it is necessary to consider the identity and nature of the diffusing species.

2.5.2 Point Defects

Solid-state diffusion involves the movement of individual particles (atoms or ions) that constitute the material. These particles are capable of movement because they vibrate around their mean positions and because the existence of defects in the solid crystal permits an occasional vibration to extend into a translation to an available lattice site nearby. Two common defects are illustrated in Fig. 2.7 for the case of a pure, single component solid: a vacancy, or unoccupied lattice site, and an interstitial atom, ie, one located between normal lattice sites.

A lattice atom can move into an adjacent vacancy, exchanging sites with the defect. Movement via this vacancy mechanism is the most common way in which diffusion occurs. Clearly, the concentration of vacancies present is important in determining the probability of atom translation occurring. The interstitial species can contribute to diffusion simply by moving into an adjacent interstitial site. This is improbable in pure metals, because the atoms are large, but operates for interstitial impurities such as C, H, N, and O dissolved in metals. Whichever the mechanism, the concentration of defects is an important factor in the particle movement rates. The question of defect concentrations is now considered.

Equilibrium concentrations of point defects in crystals are calculated by the methods of statistical thermodynamics. The application of these methods to crystals has been reviewed in detail by Schottky [14], and their use in diffusion calculations has been explored by several authors, notably Mott and Gurney

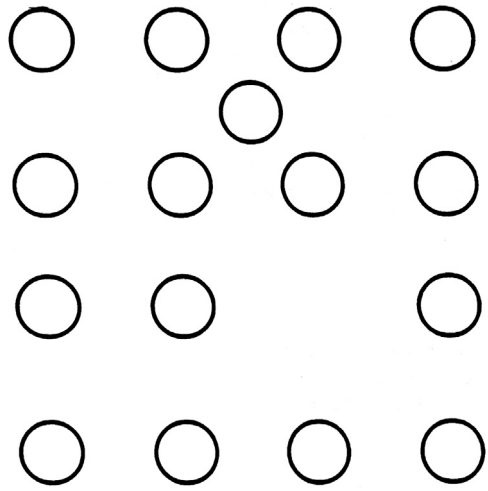

FIGURE 2.7 An individual vacancy and interstitial defect in a single component crystal lattice.

[15], Howard and Lidiard [8]. The Gibbs free energy for a monatomic crystal containing n_v vacancies and n atoms is

$$G = G_O + n_v g_v - kT \ln \frac{(n + n_v)!}{n! n_v!} \qquad [2.104]$$

where g_v is the free energy of formation of a vacancy, and the logarithmic term is recognised as the configurational entropy resulting from the presence of defects. It is this term that makes vacancy formation inevitable at all temperatures above absolute zero. The free-energy minimum representing the equilibrium state of the crystal defines the chemical potential of the vacancies as zero:

$$\left(\frac{\partial G}{\partial n_v}\right)_{T,P,N} = \mu_v = 0 \qquad [2.105]$$

Application of this to Eq. [2.103], making use of Stirling's approximation ($ln\, N! = N \ln N - N$), then yields

$$N_v = n_v/(n + n_v) = \exp(-g_v/kT) \qquad [2.106]$$

Thus Eq. [2.106] is recognised as an equilibrium expression of the same form as Eq. [2.23]. A more detailed discussion of point defect equilibria in ionic solids is provided in Chapter 3.

2.6 ABSOLUTE RATE THEORY APPLIED TO LATTICE PARTICLE DIFFUSION

We turn now to the evaluation of individual particle jump frequencies, using absolute-rate theory. The first applications to solid-state diffusion were

reported by Wert and Zener [16] and Seitz [17], and subsequent extensions for various cases have been provided by others [18–20].

When a particle moves from one lattice position to another, it passes through an intermediate state that has a higher energy because adjacent particles must be perturbed from their mean lattice positions in order to accommodate the passage of the moving particle. During this lattice distortion, an activated complex involving the two interchanging species (eg, particle plus vacancy) is formed. The activity a_{iv} of the complex is described via the equilibrium constant K_{iv} for its formation:

$$\frac{a_{iv}}{a_i a_v} = K_{iv} = \exp\left(-\frac{\Delta H_{iv}}{RT}\right)\exp\left(\frac{\Delta S_{iv}}{R}\right) \qquad [2.107]$$

where ΔH_{iv} is the enthalpy and ΔS_{iv} the entropy of complex formation.

A profile of the periodic internal-energy surface in a direction parallel to that of diffusion is shown in Fig. 2.8. An electrostatic field can be externally imposed, or can arise through the movement of the charged species themselves, and will in this case be aligned with the diffusion direction. The height of the energy barrier to the diffusion of a charged species is modified by the field, being lower for downfield movement than for upfield movement of an appropriately charged species. It will be assumed that the field does not affect ΔS_{iv}. We may write for the interchange of species i and a vacancy between planes (1) and (2) separated by a distance λ, as shown in Fig. 2.8.

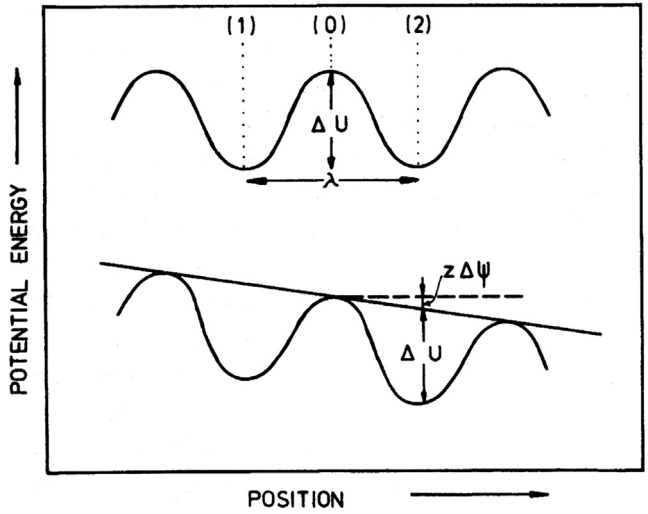

FIGURE 2.8 Potential energy profile in diffusion direction: *upper curve*, no electrostatic field, *lower curve* showing effect of electrostatic field.

$$J = m\lambda\nu_{iv}\exp\left(\frac{\Delta S_{iv}}{R}\right)\times\left\{a_i^{(1)}a_v^{(2)}\exp\left[-\frac{\Delta U_{iv}-qF\left(\psi^{(0)}-\psi^{(1)}\right)}{RT}\right]\right.$$
$$\left.-a_v^{(1)}a_i^{(2)}\exp\left[-\frac{\Delta U_{iv}-qF\left(\psi^{(2)}-\psi^{(0)}\right)}{RT}\right]\right\}\times\gamma_{iv}^{-1} \quad [2.108]$$

where m is the volume concentration of lattice sites, ν_{iv} is a kinetic frequency term, and γ_{iv} is the activity coefficient for the transition-state complex. Here q is the effective charge of the vacancy, that of the cation being zero. Superscripts in parentheses represent the location in Fig. 2.8 at which the quantity in question is evaluated.

An alternative treatment of the particle movement kinetics might be found more appealing. The rate at which ions can move from plane (1) to (2) must be proportional to the probability of finding an ion at position (1) $a_i^{(1)}$, to the availability of a vacancy for it to jump into $a_v^{(2)}$, to the frequency, ν_{iv}, with which the ion approaches the intervening energy barrier and to the Boltzmann factor giving the proportion of ions possessed of sufficient energy to surmount the barrier, $\exp(-\Delta G_{iv}/RT)$. The overall probability of the event occurring is then given by

$$\nu_{iv}a_i^{(1)}a_v^{(2)}\exp(-\Delta G_{iv}/RT)$$

Calculation of the corresponding flux from this probability by multiplying the area density of sites on plane (1), $m\lambda$, and expansion of ΔG_{iv} leads to the first term in Eq. [2.107]. The net flux is then calculated by subtracting the equivalent expression for the rate at which ions return from the second plane to the first, and Eq. [2.108] results.

To proceed, Eq. [2.108] is cleared of common terms and subjected to Taylor series expansion of the terms $a_v^{(2)}$ and $a_i^{(2)}\exp\left(-qF\psi^{(2)}/RT\right)$. Retention of linear terms, in the case where the field is not inordinately high, leads to

$$J = -\frac{m\lambda^2}{RT}\nu_{iv}K_{iv}a_ia_v\{\nabla\mu_i-\nabla\mu_v-qF\nabla\psi\} \quad [2.109]$$

which, upon substituting from Eq. [2.100], becomes

$$J = -\frac{m\lambda^2}{RT}\nu_{iv}K_{iv}a_ia_v\{\nabla\eta_i-\nabla\eta_v\} \quad [2.110]$$

Expressions of this sort always apply to pairwise site exchanges.

For the diffusion of noncharged species in a metal or an alloy, $q = 0$, we obtain

$$J_i = \frac{m\lambda^2}{RT}\nu_{iv}K_{iv}a_ia_v\{\nabla\mu_i-\nabla\mu_v\} \quad [2.111]$$

If the equilibrium condition of Eq. [2.105] is realised and the off-diagonal terms in Eq. [2.99] are ignored, this result simplifies to Eq. [2.101], with

$$L_{11} = \left(m\lambda^2/RT\right)\nu_{iv}K_{iv}a_i a_v,$$

and therefore, in the dilute (ideal) solution approximation, it is found from Eq. [2.103] that

$$D_i = \lambda^2 \nu_{iv} \exp\left(\frac{-\Delta H_{iv}}{RT}\right)\exp\left(\frac{\Delta S_{iv}}{R}\right)N_v, \qquad [2.112]$$

We now combine Eqs. [2.106] and [2.112] to determine the temperature dependence of the diffusion coefficient:

$$D = D_O \exp(-Q/RT), \qquad [2.113]$$

where $Q = \Delta H_{iv} + \Delta H_v$ with ΔH_v the enthalpy (per mole) for vacancy formation and the remaining constants have been collected in D_O. The expected Arrhenius form is arrived at and is commonly used to interpolate or extrapolate sparse experimental data.

2.7 DIFFUSION IN ALLOYS

2.7.1 Selective Oxidation and Alloy Depletion

As has been seen, successful alloy design leads to the selective oxidation of a particular alloy component, forming a slow-growing and protective oxide scale. The selective removal, or depletion, of a metal from an alloy obviously alters its average composition. This alteration is almost uniform if alloy diffusion is very fast, allowing rapid internal redistribution of the preferentially oxidising metal as a part of it is consumed. More commonly, however, diffusion is relatively slow, and the concentration of reacting metal is significantly reduced in the subsurface region of the alloy.

This phenomenon is easily observed in two-phase alloys in which the reacting metal, *B*, is concentrated in one phase. Lowering the subsurface concentration of this metal can then destabilise the B-rich phase, causing its dissolution. Metallographic images demonstrating this effect are shown in Figs 5.31 and 5.33. An example of depletion in a single-phase alloy is shown in Fig. 5.9. Here microanalysis was used to show the increase in concentration of *B* with depth into the alloy, from its strongly depleted level at the scale—alloy interface.

In order to quantify this process and predict what alloy concentration is required to withstand it, calculation of the depletion profile is required. Standard solutions to the diffusion equation for these conditions (Section 5.4) allow this to be done, provided that accurate diffusion coefficients are available.

2.7.2 Origins of Cross-Effects

For atomic diffusion in an n-component system, Eq. [2.99] may be rewritten as

$$J_i = -\sum_{j=1}^{n} L_{ij} \nabla \mu_j \qquad [2.114]$$

whence it is clear that cross-effects can arise through either kinetic interactions, as represented by the Onsager coefficients, L_{ij}, or thermodynamic interactions, represented by the variation of chemical potential with composition.

Experimental diffusion data are almost always collected in the form of concentration rather than chemical potential. For this reason, it is desirable to use a generalised form of Fick's law

$$J_i = -\sum_{j=1}^{n-1} D_{ij} \nabla C_j \qquad [2.115]$$

where the D_{ij} are functions of the kinetic coefficients L_{ij} and also reflect the dependence of chemical potential on composition. A useful example is provided by the application of Wagner's dilute solution model, Eq. [2.68]. For a ternary system, it is found that

$$\begin{aligned} D_{11} &= RT\{L_{11}(\varepsilon_{11} + 1/N_1) + L_{12}\varepsilon_{21}\}, \\ D_{12} &= RT\{L_{11}\varepsilon_{12} + L_{12}(\varepsilon_{22} + 1/N_2)\}, \\ D_{21} &= RT\{L_{22}\varepsilon_{21} + L_{21}(\varepsilon_{11} + 1/N_1)\}, \\ D_{22} &= RT\{L_{22}(\varepsilon_{22} + 1/N_2) + L_{21}\varepsilon_{12}\}, \end{aligned} \qquad [2.116]$$

In an ideal solution all $\varepsilon_{ij} = 0$, and the D_{ij} reduce to the purely kinetic form.

$$D_{ij} = RTL_{ij}/N_j \qquad [2.117]$$

For real solutions, if no kinetic cross-effects occur, ie, $L_{ij}(i \neq j) = 0$, it is clear that the diffusional cross-terms D_{ij} $(i \neq j)$ are nevertheless non-zero. In this case the dilute-solution limit (N_1, $N_2 \rightarrow 0$) may be described by

$$D_{12}/D_{11} = N_1\varepsilon_{12}/(1 + \varepsilon_{11}N_1), \qquad [2.118]$$

and

$$D_{21}/D_{22} = N_2\varepsilon_{21}/(1 + \varepsilon_{22}N_2) \qquad [2.119]$$

Thus the ternary coefficients are determined uniquely by the binary ones in dilute solutions.

For interstitial diffusion, there are negligible correlations between crystal sublattices, so that the approximation $L_{ij}(i \neq j) = 0$ is valid. Practical examples are steels Fe-C-M in which M is a substitutional metal (Si, Mn, Ni, Cr,

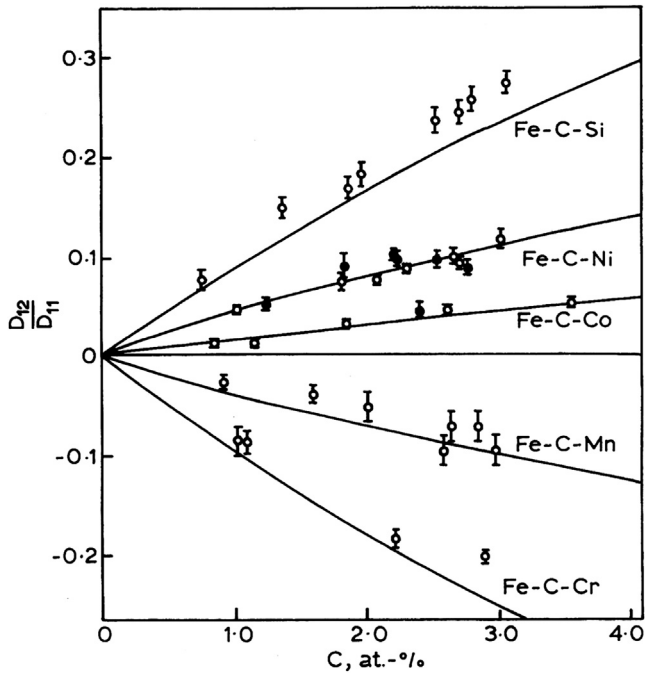

FIGURE 2.9 Variation of D_{12}/D_{11} with carbon concentration (C_1), with *solid lines* representing thermodynamic prediction. *After L.C. Brown, J.S. Kirkaldy, Trans. AIME 230 (1964) 223. Published with permission from the Minerals, Metals and Materials Society.*

Mo, Co) and the carbon is interstitial. The variation of D_{CM}/D_{CC} with carbon concentration is shown in Fig. 2.9, compared with the predictions of Eq. [2.118] using independently measured interaction parameters [21]. Agreement is quite good. Correlations of this sort can contribute to an understanding of alloy carburisation reactions.

A detailed diffusion analysis employing cross-terms was used by Nesbitt [22] in analysing the ability of Ni-Cr-Al alloys to supply aluminium to the surface to reheal damaged alumina scales. In the regime examined, the value of D_{AlCr} was as high as $0.5D_{\mathrm{AlAl}}$, leading to a significant contribution from the chromium concentration gradient to aluminium diffusion. Cross-effects between dissolved oxygen and alloy components were considered by Whittle et al. [23,24] in analysing alloy surface behaviour as oxygen diffused inwards. This analysis revealed that the cross-effect between oxygen and a selectively oxidised component was important in driving the oxygen flux. Writing the equations [2.115] as

$$J_A = -D_{AA}\nabla C_A - D_{AO}\nabla C_O$$

$$J_O = -D_{OA}\nabla C_A - D_{OO}\nabla C_O$$

we consider their application to diffusion in the subsurface zone of alloy AB, in which A is selectively oxidised. In the case of Ni-Cr at 1000°C, the self-diffusion coefficients of oxygen and chromium are of order 10^{-7} and 10^{-12} cm^2 s^{-1}, respectively, and $\nabla C_{Cr} >> \nabla C_O$. Consequently, even for small values of D_{OA}, the off-diagonal term is important, and likely predominant, in the expression for J_O.

2.7.3 Kirkendall Effect

We now examine another way in which diffusional interactions arise between components sharing the same lattice but possessing different intrinsic mobilities. Their experimental manifestation is known as the Kirkendall effect, and its measurement is used to evaluate a composite alloy diffusion coefficient defined below.

Consider a binary alloy AB in which one-dimensional diffusion occurs via atom−vacancy exchanges, and Eq. [2.111] applies to both A and B, so that D_A, D_B correspond to D_1, D_2 in Eq. [2.112]. In general the fluxes are not equal and opposite. Thus if $D_A > D_B$ in a sample initially rich in A on the left, there will be an excess flux of A from left to right over B atoms moving to the left. Consequently, the diffusion zone as a whole drifts to the left, compensating for the accumulation of matter and hydrostatic pressure that would otherwise occur on the right. Thus the lattice planes which define the frame of reference within which Eq. [2.111] applies are themselves moving. Since the diffusion zone is generally a small part of a larger sample, measurements of position that are referred to the end of the sample (the laboratory reference frame) are affected by this drift, and so, in consequence, is the estimate of diffusion rate.

The problem is the same as that faced by a navigator measuring the speed of a plane using its airspeed when a wind is blowing. A knowledge of the wind speed relative to the ground resolves the difficulty. Formally the situation is dealt with by relating the two frames of reference. In the laboratory frame of the diffusion measurement, we use

$$\sum_{i=1}^{n} J_i = 0 \qquad [2.120]$$

which is equivalent to a volume-fixed frame of reference if the partial molar volumes are approximately equal. In the lattice frame, where Eq. [2.111] applies, the expression Eq. [2.120] does not. We therefore write for the lattice frame, using J_i' to denote its fluxes,

$$J_A' + J_B' = -J_V' \qquad [2.121]$$

If the lattice frame moves with respect to the laboratory frame with a velocity v, then

$$J_i = J_i' + C_i v, \quad i = A, B, \tag{2.122}$$

where the nonprimed fluxes refer to the laboratory frame. These equations are solved using Eq. [2.120] to obtain

$$v = \frac{-J_A' + J_B'}{C_A + C_B} \tag{2.123}$$

or, upon resubstitution,

$$J_A = -J_B = N_B J_A' - N_A J_B' \tag{2.124}$$

In the simple situation in which the off-diagonal Onsager coefficients are set equal to zero, and local equilibrium applies ($\nabla \mu_v = 0$), Eqs [2.111] and [2.112] simplify to Fick's law Eq. [1.24]. Since, moreover, for an isobaric system in which partial molar volumes $\overline{V}$ are equal

$$\overline{V}(C_A + C_B) = 1 \tag{2.125}$$

a combination of Eqs. [2.123]–[2.125], and Eq. [1.24] yields

$$v = \overline{V}(D_A - D_B)\frac{\partial C}{\partial x} \tag{2.126}$$

$$J_A = -(N_B D_A + N_A D_B)\frac{\partial C_A}{\partial x} \tag{2.127}$$

The value of v can be measured using inert markers, as is now discussed.

The first demonstration of lattice drift was performed by Smigelskas and Kirkendall [25] using the diffusion arrangement shown schematically in Fig. 2.10. Molybdenum wires (the markers) were attached to a block of brass (Cu-Zn) and then an outer copper layer was applied by electroplating. Annealing this couple at high temperature caused rapid outward diffusion of the more mobile zinc from the brass into the copper, slower inward diffusion of copper, and inward drift of the molybdenum markers. The effect is quite general and is widely used in diffusion measurements.

For an infinite diffusion couple (sample much larger than the diffusion zone), it can be shown that

$$C_A = C_A(\lambda), \quad \lambda = x/t^{1/2} \tag{2.128}$$

and hence

$$v = \frac{D_A - D_B}{t^{1/2}}\frac{dC_A}{d\lambda} \tag{2.129}$$

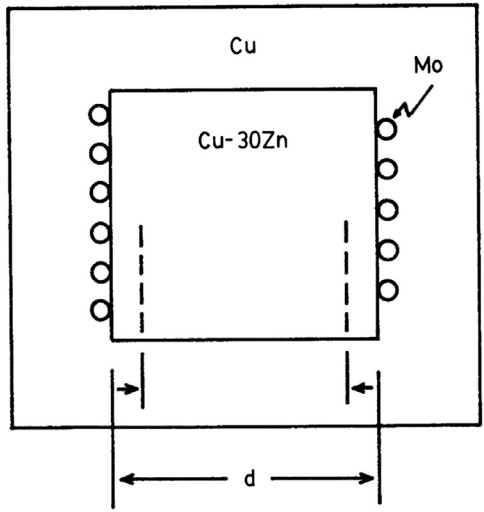

FIGURE 2.10 Lattice drift experiment of Smigelskas and Kirkendall.

Because the markers are located at a point of fixed composition and therefore at a fixed value of $dC_A/d\lambda$, Eq. [2.129] integrates immediately to yield

$$x_m = 2(D_A - D_B)\frac{dC_A}{d\lambda}t^{1/2} \qquad [2.130]$$

for the marker displacement. The quantities D_A, D_B are known as the intrinsic diffusion coefficients because they refer to diffusion with respect to the lattice planes in the presence of an activity gradient. It is necessary now to relate these to the measured tracer coefficients, D_{A^*}, D_{B^*}. These refer to the diffusional intermixing of different isotopes of the same atom or ion, and usually the enthalpy of mixing is small and the solution ideal. In this case, Eq. [2.103] simplifies to

$$D_1 = L_{11}RT/C_1 \qquad [2.131]$$

On the other hand, the intrinsic diffusion coefficient refers to a nonideal solution and Eq. [2.103] must be used without approximation. As a result

$$D_A = D_{A^*}\left(1 + \frac{d\ln\gamma_A}{d\ln N_A}\right) \qquad [2.132]$$

Using the Gibbs–Duhem equation for equilibrium in a solution (Eq. [2.46]), we may write

$$1 + \frac{d\ln\gamma_A}{d\ln N_A} = 1 + \frac{d\ln\gamma_B}{d\ln N_B} \qquad [2.133]$$

then Eq. [2.127] becomes

$$J_A = -\widetilde{D}\nabla N_A \qquad [2.134]$$

with

$$\widetilde{D} = (N_B D_{A^*} + N_A D_{B^*})\left(1 + \frac{d\ln\gamma}{d\ln N}\right) \qquad [2.135]$$

This is the Darken–Hartley–Crank equation [26,27], and $\widetilde{D}$ is the *chemical diffusion coefficient*. The quantity $\widetilde{D}$ is also called the alloy diffusion coefficient, and is obtained from a diffusion couple measurement (Section 2.8). If markers are used in the measurement, values of the self-diffusion coefficients D_A, D_B may also be obtained. This provides a powerful technique for exploring the compositional dependence of the D_i.

The above analysis has been extended to multicomponent systems (see, eg, [12]). The lack of balance among the intrinsic diffusive flows always leads to a compensating mass flow of material. That is to say, diffusional cross-effects arise even in the absence of kinetic or thermodynamic correlations. Thus even a component with a negligible intrinsic mobility will move. The simple form of Fick's law fails, and the generalised form Eq. [2.115] must be used.

2.8 DIFFUSION COUPLES AND THE MEASUREMENT OF DIFFUSION COEFFICIENTS

In the most common diffusion measurements, the movement of a system toward homogeneity is observed and compared with the predictions of the diffusion equations. These equations, together with appropriate boundary conditions, yield solutions for the one-dimensional case of the general form

$$C_i = C_i(x, t, D) \qquad [2.136]$$

Thus D is evaluated by fitting the expressions to experimental data $C_i = C_i(x,t)$. We consider here *diffusion couple* experiments in which two different homogeneous mixtures are brought into contact at a planar interface and diffusion observed along a direction normal to it.

Two types of diffusion couples are important. If sample dimensions and the period of diffusion are such that concentrations at the ends of the sample do not change, then the experiment is described as an infinite diffusion couple. These couples are used to measure chemical diffusion. In a tracer diffusion measurement, the couple consists of a homogeneous block of material and a thin film of isotopically labelled but compositionally identical material. The two types of diffusion couple are shown schematically in Fig. 2.11. Predicted profiles of the form Eq. [2.136] are obtained from Fick's law (Eq. [1.24]), which is subject to the continuity condition

$$\frac{\partial C_i}{\partial t} = -\frac{\partial J_i}{\partial x} \qquad [2.137]$$

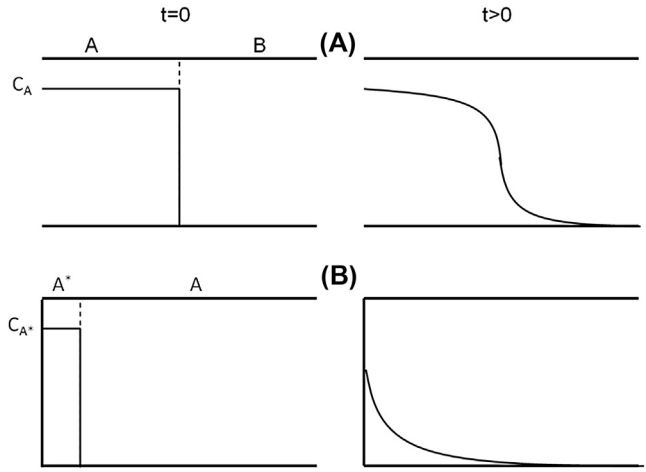

FIGURE 2.11 Diffusion couples before and after diffusion: (A) infinite couple (B) thin film (tracer experiment) couple.

leading to Fick's Second law

$$\frac{\partial C_i}{\partial t} = D\frac{\partial^2 C_i}{\partial x^2} \qquad [2.138]$$

where D has been approximated as constant. The solution of Eq. [2.138] is required for the appropriate boundary and initial conditions. Methods and a number of solutions are available from Carslaw and Jaeger [28] and Crank [29]. The thin film solution applies to the one-dimensional tracer diffusion experiment of Fig. 2.11B:

$$C(x,t) = \frac{\alpha \exp(-x^2/4D_{A^*}t)}{2(\pi D_{A^*}t)^{1/2}} \qquad [2.139]$$

where α is the amount of labelled material per unit area of film. After annealing, the couple is sectioned and the tracer concentration measured as a function of position. The value of D_{A^*} is then evaluated from a logarithmic plot according to Eq. [2.139].

For an infinite diffusion couple consisting initially of one-half containing a uniform concentration C_0 and the other a concentrationC_1 (Fig. 2.11A), after diffusion time t, we have

$$\frac{C(x,t) - C_0}{C_1 - C_0} = \frac{1}{2}\left[1 - \mathrm{erf}\left(x/2\sqrt{Dt}\right)\right] \qquad [2.140]$$

where erf is the Gaussian error function,

$$\mathrm{erf}(z) = \frac{2}{\sqrt{\pi}}\int_0^z \exp\left(-u^2\right)du \qquad [2.141]$$

Corresponding solutions are available for ternary systems [12]. Properties of the error function together with an abbreviated table of its values are shown in Appendix C.

The above solutions rely on D being constant. This will apply in the tracer diffusion case, and Eq. [2.139] can be used directly. However, it is improbable in the presence of a concentration gradient, the situation obtaining for the diffusion couple described by Eq. [2.140] and Fig. 2.11A. Either the difference C_1-C_0 must be kept small, or the analysis of Boltzmann [30] and Matano [31] must be used in this case. Here the new variable $\lambda = x/\sqrt{t}$ is introduced. The initial conditions for the infinite diffusion couple $C = C_0$ for $x < 0$ and $C = 0$ for $x > 0$ at $t = 0$ are independent of x, apart from the discontinuity at $x = 0$ (Fig. 2.11A). They can be described as $C = C_0$ at $\lambda = -\infty$ and $C = 0$ at $\lambda = +\infty$, and the Boltzmann–Matano analysis applies. Fick's Law can then be transformed into an ordinary differential equation

$$-\frac{\lambda}{2}\frac{dC}{d\lambda} = \frac{d}{d\lambda}\left(D\frac{dC}{d\lambda}\right),$$

which integrates between zero and a value C' such that $0 < C' < C_0$, and for a fixed value of t, to yield

$$-\frac{1}{2}\int_{C=0}^{C=C'} x\,dC = Dt\left[\frac{dC}{dx}\right]_{C=0}^{C=C'}$$

Noting that $dC/dx = 0$ at $c = 0$ and $c = C_0$, we arrive at the final solution

$$\widetilde{D}(C') = -\frac{1}{2}\left(\frac{d\lambda}{dC}\right)\int_0^{C'} \lambda\,dC \qquad [2.142]$$

with

$$\int_{C_0}^{C_1} x\,dC = 0 \qquad [2.143]$$

defining the origin of coordinates. Graphical or numerical evaluations of the differential and the integral in Eq. [2.142] are used to evaluate $\widetilde{D}(C')$, as shown in Fig. 2.12. Observation of marker movement in the diffusion couple then allows calculation of the self-diffusion coefficients D_A,D_B from Eq. [2.130]–[2.135].

2.8.1 Diffusion Data for Alloys

It is often expedient to ignore diffusional interactions, either because the necessary data are not available or because an approximate calculation is all that is required. In such cases, we rely on self-diffusion coefficients, usually

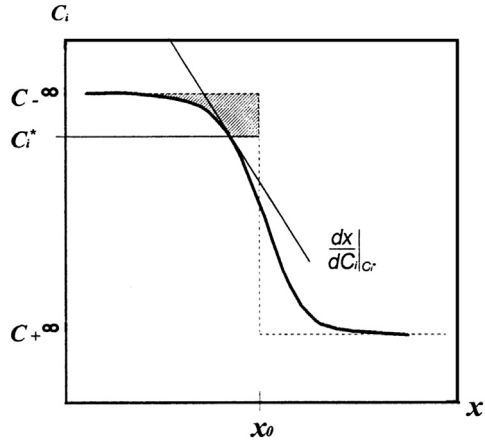

FIGURE 2.12 Concentration profile in infinite couple after diffusion, showing how the quantities required for the Boltzmann–Matano analysis Eq. [2.142] are evaluated.

measured on binary alloys. These apply to either substitutional (vacancy exchange) diffusion of metal components or interstitial diffusion of solute oxidants. Most measurements have been carried out using tracer diffusion experiments. These are related to the intrinsic, or self-diffusion, coefficients through Eq. [2.132] which, in a near ideal solution, approximates to

$$D_A \approx D_{A^*}$$

In some cases not even tracer data are available, but a chemical diffusion coefficient $\widetilde{D}$ may have been measured. If the diffusing species of interest is both dilute and highly mobile, then the expression

$$\widetilde{D} = N_A D_B + N_B D_A$$

can be approximated as

$$\widetilde{D} = D_B$$

A selection of self-diffusion coefficient data for binary alloys is given in Appendix D. For multicomponent systems where Eq. [2.115] holds, the Matano analysis can also be applied. The origin is then defined by the condition Eq. [2.143] being simultaneously satisfied for all components. Data are available for a number of ternary alloy systems in a useful review compiled by Dayananda [32].

A rather different treatment is required for diffusion in ionic solids, where the charges on individual species must be explicitly recognised. This is dealt with in Chapters 3 and 5.

2.9 INTERFACIAL PROCESSES AND GAS PHASE MASS TRANSFER

As seen earlier, linear oxidation kinetics are expected if a surface or interfacial process is rate controlling. We consider the scale−gas interface, examining first the situation where the supply of oxidising gas is not rate determining, and gas adsorption equilibrium can be expected. The very initial reaction between gas and bare metal is not considered here. Instead, a uniform oxide scale is assumed to have already formed.

2.9.1 Gas Adsorption

The reaction may be written as

$$\begin{aligned} &O_2(g) + S = O_2|S && (a)\\ &O_2|S + S = O|S + O|S && (b)\\ &O|S \xrightarrow{k_c} \text{Oxide} && (c) \end{aligned}$$

where S denotes a surface site, $O_2|S$ and $O|S$ adsorbed molecules and atoms and k_c the rate constant for the slow step (c). The pre-equilibria (a) and (b) lead to

$$[O_2|S] = [S]K_a p_{O_2} \qquad [2.144]$$

$$[O|S] = ([S]K_b[O_2|S])^{\frac{1}{2}} \qquad [2.145]$$

where square brackets indicate area concentration. Substitution of Eq. [2.144] into Eq. [2.145] leads to

$$[O|S] = [S](K_aK_b)^{\frac{1}{2}}p_{O_2}^{\frac{1}{2}} \qquad [2.146]$$

Assuming now that the surface area and total concentration of sites are constant:

$$M = [S] + [O_2|S] + [O|S] \qquad [2.147]$$

and substituting from Eq. [2.144] and [2.146], one obtains

$$[S] = M \Big/ \left\{1 + K_a p_{O_2} + (K_aK_b)^{\frac{1}{2}}p_{O_2}^{\frac{1}{2}}\right\} \qquad [2.148]$$

The constant M is of order 10^{15} cm^{-2}. Combination of Eqs [2.146] and [2.147] and the rate equation for reaction (c) then leads to the result

$$\text{Rate} = \frac{k_c M(K_aK_b)^{\frac{1}{2}}p_{O_2}^{\frac{1}{2}}}{1 + (K_aK_b)^{\frac{1}{2}}p_{O_2}^{\frac{1}{2}}\left[1 + (K_a/K_b)^{\frac{1}{2}}p_{O_2}^{\frac{1}{2}}\right]} \qquad [2.149]$$

The rate is of course constant at fixed p_{O_2}, but varies in a complex way with oxygen potential.

Three limiting cases can be seen. At sufficiently low values of p_{O_2}, $K_a p_{O_2} << 1 >> \left(K_a K_b p_{O_2}\right)^{\frac{1}{2}}$ so that

$$\text{Rate} = k_c \text{M} (K_a K_b)^{\frac{1}{2}} p_{O_2}^{\frac{1}{2}} \quad [2.150]$$

At higher p_{O_2} values, the competitive adsorption of molecular and atomic oxygen must be considered. When atomic adsorption predominates over the molecular form

$$(K_a/K_b)^{\frac{1}{2}} p_{O_2}^{\frac{1}{2}} << 1 \quad [2.151]$$

and the term in square brackets in the denominator approximates to unity. If, furthermore, the surface is saturated, ie,

$$(K_a K_b)^{\frac{1}{2}} p_{O_2}^{\frac{1}{2}} >> 1 \quad [2.152]$$

then the oxidation rate is simply

$$\text{Rate} = k_c \text{M} \quad [2.153]$$

and independent of oxygen partial pressure. However, if molecular adsorption predominates, the converse of Eq. [2.151] is true and the rate equation becomes

$$\text{Rate} = \frac{k_c \text{M} (K_a K_b)^{\frac{1}{2}} p_{O_2}^{\frac{1}{2}}}{1 + K_a p_{O_2}} \quad [2.154]$$

If the surface is close to saturation with molecular oxygen, $K_a p_{O_2} >> 1$, then an inverse dependence of the rate on p_{O_2} is predicted.

Competitive adsorption treatments are particularly useful in analysing oxidation kinetics in more complex gases such as $CO + CO_2$ mixtures [33], but they have also been used for oxygen alone [34], where the competing species are O and O_2.

Adsorption equilibrium can only be supported if gas species arrive at the scale surface quickly enough to keep up with reaction (c). This may not be the case if the oxidant partial pressure is very low. Two such situations are of interest: pure oxidant at low pressure, and oxidant as a dilute component of an otherwise inert gas.

2.9.2 Gas Phase Mass Transfer at Low Pressure

This situation is described using the Hertz–Langmuir–Knudsen equation, which derives from the kinetic theory of gases [35]. In the ideal case,

$$k_i = \frac{p_i}{(2\pi m_i k T)^{\frac{1}{2}}} \quad [2.155]$$

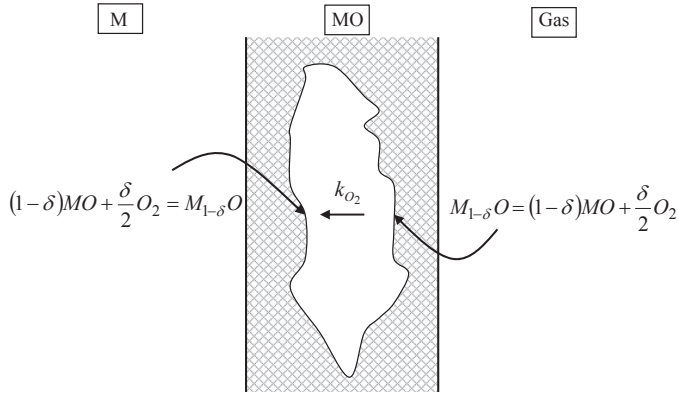

FIGURE 2.13 Vapour phase mass transport inside pores within a growing scale.

where k_i is the rate, p_i the partial pressure, m_i the mass of a molecule of species i and k is Boltzmann's constant. This expression describes both the rate of arrival of a low pressure gas at a flat surface and, equally, the rate of evaporation into a vacuum of the same species. Using practical units of g cm^{-2} s^{-1} for k_i and atm for p_i, the rate is calculated as

$$k_i = 44.3 p_i (\mathrm{MW}_i/T)^{\frac{1}{2}} \qquad [2.156]$$

where MW_i is the species molecular weight.

This equation can be used to investigate gas phase mass transfer inside porous or cracked oxide scales, as shown schematically in Fig. 2.13. The question addressed is whether the values of p_{O_2} expected from local equilibrium with the surrounding oxide can sustain significant mass transfer across the cavities to support oxide growth. If the oxide is FeO at 1000°C, then the equilibrium p_{O_2} is in the range $1 \times 10^{-15} - 2.8 \times 10^{-13}$ atm. Oxygen transfer rates calculated from Eq. [2.156] are found to be $7 \times 10^{-15} - 2 \times 10^{-12}$ g cm^{-2} s^{-1}, corresponding to a thickness of wüstite grown on the inner side of the cavity at rates of about 1−100 nm per year. Thus closed pores and cracks are seen to be effective local barriers to continued scale growth if O_2 is the only vapour species within them.

2.9.3 Mass Transfer in Dilute Gases

The usual situation encountered in practice and in the laboratory is a gas mixture flowing past a metal surface. The Hertz−Langmuir−Knudsen equation cannot be used in this situation because of the multiple collisions occurring between oxygen and other molecules. The rate of transfer is governed by the gas flow rate, the width of the gas boundary layer (which is retained by viscous drag), oxygen partial pressure and gas mixture properties.

A readable account of how this problem is solved has been provided by Gaskell [35].

The flux of oxygen to a flat surface from a gas flowing parallel to it is given by

$$J = \frac{k_m}{RT}\left(p^{(o)} - p^{(i)}\right) \qquad [2.157]$$

where k_m is a mass transfer coefficient and $p^{(o)}$, $p^{(i)}$ are the oxygen partial pressures in the bulk gas and at the solid surface, respectively. The mass transfer coefficient is given by

$$k_m = 0.664\left(\frac{D_{AB}^4}{\nu_g}\right)^{1/6}\left(\frac{\nu}{L}\right)^{\frac{1}{2}} \qquad [2.158]$$

where D_{AB} is the diffusion coefficient in a binary gas A-B, ν_g the kinematic viscosity, ν the linear velocity of the gas and L the length of surface. The diffusion coefficient is found from the Chapman−Enskog formulation [36,37] of the kinetic theory of gases.

$$D_{AB} = \frac{1.858 \times 10^{-3}\sqrt{T^3(1/\mathrm{MW}_A + 1/\mathrm{MW}_B)}}{P\sigma_{AB}^2\Omega_{D,AB}} \qquad [2.159]$$

Here MW_A, MW_B are the molecular weights of the two gas species, σ_{AB} their average collision cross-section, $\Omega_{D,AB}$ a collision integral, and the numerical factor arises from the use of non-SI units. These are $\mathrm{cm}^2\ \mathrm{s}^{-1}$ for D_{AB}, Å for σ, Poise for η and atm for P, with a dimensionless Ω. Tabulations of σ and the data permitting calculation of Ω_D are available [35,38]. The kinematic viscosity is defined as

$$\nu_g = \eta_g/\rho \qquad [2.160]$$

where ρ is the gas density, here in $\mathrm{g\ cm}^{-3}$, and the viscosity, η_g, is given by

$$\eta_g = \frac{2.669 \times 10^{-5}\sqrt{MT}}{\sigma^2\Omega} \qquad [2.161]$$

with Ω a different collision integral, tabulated values of which are also available. The description is valid when the dimensionless Schmidt number

$$S_c = \nu/D \qquad [2.162]$$

has a value between 0.6 and 50.

The oxidation of steel in reheat atmospheres considered in Section 1.1 provides an example where this description can be used. Laboratory simulations of reheat furnace gases have been used [39] to investigate the effect of combustion stoichiometry on steel scaling rates at 1100°C. The equilibrium gas composition corresponding to the combustion of methane with 1% excess air is shown in Table 2.3. Reaction of a low carbon steel with this gas produced

TABLE 2.3 Equilibrium Partial Pressures and Corresponding Oxygen Transport Rates in 101% Stoichiometric Combustion Gas at 1100°C [39].

	CO_2	CO	N_2	O_2	H_2O	H_2
p/atm	9.42×10^{-2}	1.3×10^{-6}	0.72	1.9×10^{-3}	0.188	1.3×10^{-6}
J_O/mol cm^{-2} s^{-1}	5×10^{-7}			1.2×10^{-8}	1×10^{-6}	

a scale consisting of single-phase FeO, which thickened according to linear kinetics. These are not the results to be expected if local equilibrium at the scale—gas interface was achieved. In that case, the surface oxide would be Fe_3O_4, an additional layer of FeO would grow beneath it, and diffusion-controlled, parabolic kinetics would result. The situation at the scale—gas interface therefore requires analysis.

Gas phase mass transfer rates calculated from Eqs. [2.157] and [2.158] are shown in Table 2.3. The measured oxidation rate corresponded to $J_O = 2 \times 10^{-7}$ mol O/cm^2s. As is clear from the comparison, molecular oxygen was not a significant reactant species, as its gas-phase mass transfer rate was too slow to keep up with the scaling rate. On the other hand, gas-phase transport of H_2O and CO_2 was more than fast enough to sustain the observed oxidation rate. Thus it is concluded on this basis that H_2O and/or CO_2 were the reactants, but that gas-phase transport was not rate controlling, because of the relative abundance of these species. This conclusion was confirmed by the magnitude of the activation energy for the linear rate constant, measured as 135 kJ mol^{-1}. This value is much greater than the temperature effect predicted from Eqs. [2.157] and [2.158]. Other measurements [40] of linear steel oxidation rates in dilute O_2-N_2 gases, where the rate is controlled by gaseous mass transfer, yielded an apparent activation energy of 17 kJ mol^{-1}. Thus it is eventually concluded that the rate-controlling step in the linear oxidation process observed in this combustion gas at 1100°C is a surface reaction.

As seen above, quantitative gas phase mass transfer calculations can be useful in determining the feasibility of vapour transport within closed scale voids and cracks, in identifying reactant species in gas mixtures and in distinguishing the contributions to rate control by mass transfer and interfacial reactions.

2.10 MECHANICAL EFFECTS: STRESSES IN OXIDE SCALES

Oxide scales are usually subject to mechanical stress. This is of interest, because if the oxide stress is high enough, the scale will deform or even fracture. In the absence of external loading a compressive stress in the oxide is

balanced by a tensile one in the metal. Thus the mechanical state of the oxide reflects changes occurring in both phases. It is convenient to divide these into two classes: stresses developed during oxidation and those developed during temperature change. These matters have been reviewed several times, and the reader is referred in particular to Stringer [41], Taniguchi [42], Stott and Atkinson [43], Evans [44] and Schutze [45].

2.10.1 Stresses Developed During Oxidation

Oxidation causes volume changes which, if constrained by specimen shape or constitution, are accommodated by deformation or strain in the oxide, ε_{ox}. Pilling and Bedworth [46] considered scale growth occurring by inward oxygen transport and recognised that if the ratio V_{ox}/V_m was greater than one, the resulting expansion could put the oxide into compression, whereas if the ratio was less than unity, tension and a discontinuous oxide could result.

In the practically relevant case of $V_{ox}/V_m > 1$, if the scale grows by outward metal diffusion, a new oxide is formed at the free, unconstrained oxide−gas interface, and no strain results. However, if the scale grows by inward oxygen diffusion, the volume change accompanying new oxide formation has to be accommodated at the metal−oxide interface, leading to

$$\varepsilon_{ox} = \left[(V_{ox}/V_m)^{\frac{1}{3}} - 1 \right] \qquad [2.163]$$

if no other stress-relieving mechanism is available. If the oxide behaves elastically, the corresponding growth stress would be

$$\sigma_{ox} = \frac{-E_{ox}}{1 - \nu_P} \varepsilon_{ox} \qquad [2.164]$$

where E_{ox} is the elastic modulus and ν_P is Poisson's ratio for the oxide.

The Pilling−Bedworth description is conceptually useful but of little quantitative use. Firstly, many oxides grow predominantly by outward metal diffusion, and the model does not apply. Even in the case of inward diffusion, the stress levels calculated from Eqs [2.163] and [2.164] are found to be impossibly high [47]. The solution to this problem is proposed [45] to be mixed diffusion of both metal and oxide, leading to the growth of new oxide both at the scale surface and within its interior. Mixed transport can become possible as a result of grain boundaries or microcracks facilitating oxygen access. The relative contributions of the different growth sites are expected to vary with the factors affecting individual metal and oxygen transport mechanisms (T, p_{O_2}, oxide grain size and substrate preparation). In his review [48] of the extensive data available for chromium oxidation, Kofstad demonstrated that the Cr_2O_3 scale grows by counter-current diffusion of metal and oxygen along grain boundaries. The formation of a new oxide in the boundaries results in lateral stress development, deformation of the scale and its partial

detachment from the metal surface. Plastic deformation increases with decreasing oxygen activity and smaller grain size.

Using the assumption of elastic oxide behaviour, Srolowitz and Ramanarayanan [49] analysed the effect of new oxide growth at grain boundaries within the scale. When the grain size $\delta << X$, they find

$$\sigma_{ox} = \frac{4G_{\text{ox}}d_i}{2\delta(1-2\nu_P)} \qquad [2.165]$$

where G_{ox} is the shear modulus of the oxide and d_i the width of new oxide grown at internal grain boundaries.

Additional stresses arise when curved metal surfaces are oxidized. Consider first an infinite plane metal surface being oxidised, with $V_{\text{ox}}/V_M > 1$. As metal is consumed, the metal−oxide interface recedes. The oxide scale, which is chemically bonded to the metal surface, remains attached and moves with the retreating metal. If scale growth is sustained wholly by metal transport, no stress results. Consider now a convex metal surface oxidising and receding. As the oxide follows it, it is compressed tangentially into the smaller volume formerly occupied by metal. Simultaneously, a radial tensile stress develops. The differing consequences for concave and convex slopes, inward and outward diffusion and $V_{\text{ox}}/V_M >$ or < 1 have been explored by Hancock and Hurst [50] and Christ et al. [51]. The qualitative results for $V_{\text{ox}}/V_M > 1$ are illustrated in Fig. 2.14.

Oxide stresses can also be caused in other ways during oxidation. Dissolution of oxygen into metals with high solubilities (eg, Ta, Ti) can cause large expansions [52]. Internal precipitation of oxides [53] or oxidation of internal carbides [54] in alloy subsurface regions can cause very large volume expansions and tensile stresses in external scales. Phase changes in an alloy resulting from selective oxidation also causes volume changes. In general, any deformation of the substrate metal, including that due to external loading, is transferred to an adherent scale because

$$\varepsilon_{\text{ox}} = \varepsilon_M \qquad [2.166]$$

for an intact scale.

2.10.2 Stresses Developed During Temperature Change

Metals and oxides can have significantly different coefficients of thermal expansion, α, as seen in Table 2.4. The stress produced in an intact, adherent scale by a temperature change, ΔT, is given by [55]

$$\sigma_{\text{ox}} = \frac{-E_{\text{ox}}\Delta T(\alpha_M - \alpha_{\text{OX}})}{\frac{E_{\text{ox}}}{E_M}\frac{X_{\text{ox}}}{X_M}\left(1-\nu_P^{(M)}\right)+\left(1+\nu_P^{(\text{OX})}\right)} \qquad [2.167]$$

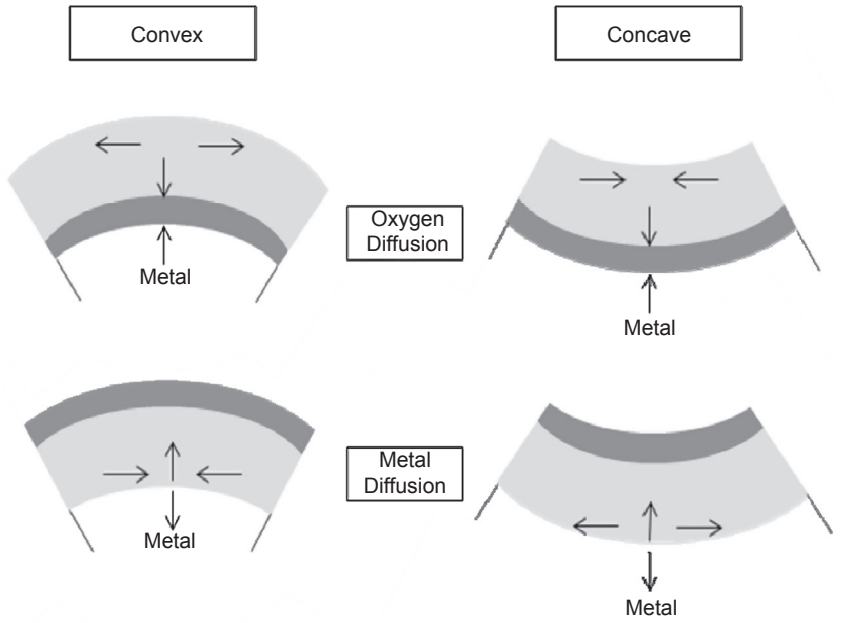

FIGURE 2.14 Effect of metal surface curvature on growth stress development in oxide scales. *Based on P. Hancock, R.C. Hurst, in: M.G. Fontana, R.W. Staehle (Eds.), Advances in Corrosion Science and Technology, vol. 4, Plenum, New York, 1974, p. 1; W. Christ, A. Rahmel, M. Schütze, Oxid. Met. 31 (1989) 1.*

where X_{ox}, X_M are the thicknesses of scale and substrate metal, $\nu_P^{(OX)}$ and $\nu_P^{(M)}$ are the Poisson's ratio values for scale and metal and the values of E and α have been approximated as independent of temperature. For thin scales on thick substrates, Eq. [2.167] is adequately approximated by

$$\sigma_{ox} = \frac{-E_{ox}\Delta T(\alpha_M - \alpha_{OX})}{1 - \nu_P^{OX}} \qquad [2.168]$$

providing that linear elastic behaviour is in effect.

Clearly, the thermally induced stress is dependent on the magnitude of the temperature change and the difference between coefficients of thermal expansion. As seen in Table 2.4, values for metals are usually greater than for oxides, and rapidly cooling an oxidized metal from a high temperature will put the scale in compression. If the resulting stress is high enough, the scale suffers mechanical failure. The tabulated data explain why such failure is rare for oxide scales on nickel and cobalt, but common for Cr_2O_3 scales on austenitic chromia-forming materials such as Alloy 800.

The development of stresses, both during oxidation and during temperature change, has been described here in terms of linear elastic behaviour. Thus it has

TABLE 2.4 Coefficients of Thermal Expansion (α)

Material	$10^6\alpha/K^{-1}$	T-range/°C	References
Fe	15.3	0–900	[59]
FeO	15.0	400–800	[60]
FeO	12.2	100–1000	[59]
Fe_2O_3	14.9	20–900	[59]
Ni	17.6	0–1000	[59]
NiO	17.1	20–1000	[59]
Co	14.0	25–350	[59]
CoO	15.0	20–900	[59]
Cr	9.5	0–1000	[59]
Cr_2O_3	7.3	100–1000	[59]
Cr_2O_3	8.5	400–800	[60]
Alloy 800	16.2–19.2	20–1000	[45]
12 Cr, 1 Mo steel	10.8–13.3	20–600	[45]
α-Al_2O_3 (single xl)	5.1–9.8	28–1165	[61]
Kanthal	15	20–1000	Kanthal AB

been assumed that no stress relief mechanisms are in effect. This is, in fact, not the case, and a variety of outcomes can be arrived at. Stress can be relieved by plastic deformation, a process which occurs at low temperatures by dislocation movement, and at high temperature by creep. The latter is a time-dependent material flow resulting from lattice diffusion (Nabarro-Herring creep [56,57]) or grain boundary diffusion (Coble creep [58]). Creep processes are strongly dependent on grain size and impurities, and in oxides, to some extent, on oxygen activity. An example where the stresses at a sample corner have been relieved by creep in the alloy is shown in Fig. 2.15. If the stresses in an oxide scale develop to levels larger than can be accommodated by elastic strain, and if plastic deformation is insufficient to relieve the stresses, mechanical disruption of the system results. Depending on its stress state, properties and microstructure (which can change with temperature), the scale can fracture, form multiple microcracks, disbond from the metal (or separate along scale layer interfaces) or spall. Spallation means the separation and ejection of fragments from the scale and is illustrated in Fig. 2.16. The situation is analysed using a fracture mechanics approach, on the highly probable

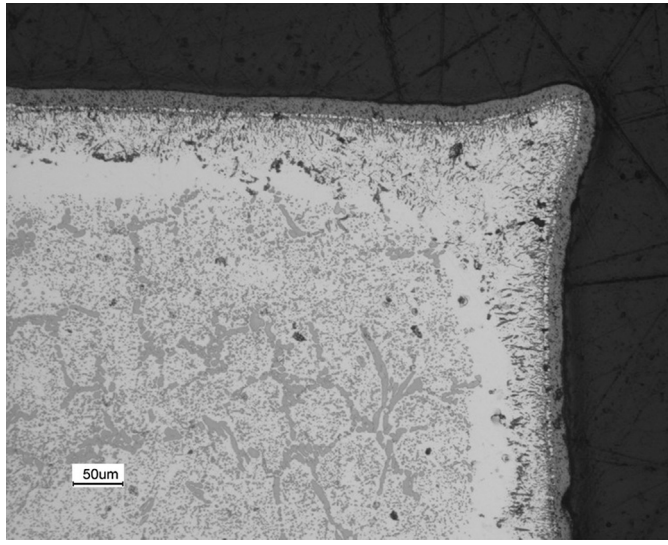

FIGURE 2.15 Deformation of cast, heat-resisting steel sample corner during oxidation at 1100°C.

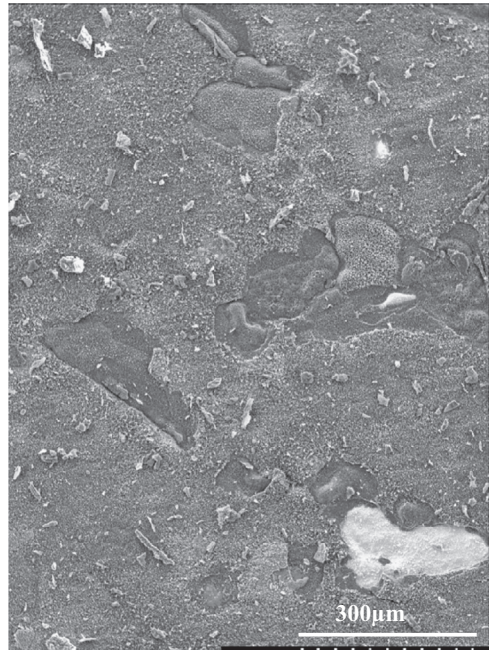

FIGURE 2.16 Partial spallation of alumina scale from platinum-modified nickel aluminide coating system resulting from temperature cycling between 1200°C and 80°C.

assumption that small defects are always present in the scale. The energy available from releasing the stress by growing a crack is compared with the energy required to form the newly created surfaces. In the linear-elastic regime, the critical stress, σ_c, is found in a simple calculation to be given by

$$\sigma_c\sqrt{\pi a} = \sqrt{G_c E'} \qquad [2.169]$$

where a denotes the geometric dimensions of a pre-existing defect (length of a surface crack or half-length of an internal crack), G_c is the energy needed to create new surface and E' is the effective elastic modulus. The left side of Eq. [2.169] represents the stress intensity factor, and the right side the fracture toughness of the material. Measured values of the latter are found [44] to be of order 1 MPa $m^{1/2}$ for oxide scales.

For a much more detailed discussion of the mechanical properties of oxide scales, the reader is referred to the book by Schütze [45]. Mechanical failure of scales leading to their spallation and the consequential acceleration in alloy failure rates are discussed in detail in Chapter 11. Alloy design strategies for minimizing spallation are considered in Section 7.5.

FURTHER READING

Chemical Thermodynamics and Phase Equilibria

The Principles of Chemical Equilibrium: with Applications in Chemistry and Chemical Engineering, 4th ed., by K. Denbigh, Cambridge University Press (1997).

Introduction to the Thermodynamics of Materials, 5th ed., by D.R. Gaskell, Taylor and Francis, New York, NY (2008).

Chemical Thermodynamics of Materials, by C.H.P. Lupis, North Holland, New York (1983).

Materials Thermochemistry, 6th ed., by O. Kubaschewski, C. B. Alcock and P.J. Spencer, Pergamon Press (1993).

Thermodynamics of Solids, 2nd ed., by R.A. Swalin, Wiley-Interscience, New York (1972).

Thermodynamics and an Introduction to Thermostatics, 2nd ed., by H.B. Callen, Wiley, New York (1985).

Phase Equilibria, Phase Diagrams and Phase Transformations, Their Thermodynamic Basis, 2nd ed., by M. Hillert, Cambridge University Press (2008).

Constitution of Binary Alloys, 2nd ed., M. Hansen, McGraw-Hill, New York (1958). See also: First supplement, R.P. Elliott (1965); Second supplement, F.A. Shunk (1969).

Phase Diagrams for Ceramists, by E.M. Levin, C.R. Robbins and H.F. McMurdie, 2nd ed., American Ceramic Society, Inc., Columbia, OH (1969). See also supplements (1969, 1975).

Diffusion in Solids

Electronic Processes in Ionic Crystals, by N.F. Mott and R.W. Gurney, Dover Publications (1964).
Atom Movements, ed. J.H. Holloway, ASM, Cleveland (1951).
Diffusion in and Through Solids, by R.M. Barrer, Cambridge University Press (1951).
Diffusion in Solids, 2nd ed., by P.G. Shewmon, Wiley (1991).
Atom Movements: Diffusion and Mass Transport in Solids, by J. Philibert, Les Editions de Physique (1991).
Diffusion in Solids: Fundamentals, Methods, Materials, Diffusion Controlled Processes, by H. Mehrer, Springer, Berlin (2007).
Fundamentals of Grain and Interphase Boundary Diffusion, 2nd ed., by I. Kaur and W. Gust, Ziegler Press, Stuttgart (1989).
Diffusion in the Condensed State, by J.S. Kirkaldy and D.J. Young, Institute of Metals, London (1987).

Point Defects in Solids

Electronic Processes in Ionic Crystals, by N.F. Mott and R.W. Gurney, Dover Publications (1964).
The Chemistry of Imperfect Crystals, 2nd ed., by F.A. Kroger, North Holland, Amsterdam (1973).
Nonstoichiometry, Diffusion and Electrical Conductivity in Binary Metal Oxides, by P. Kofstad, Wiley-Interscience, New York (1972).
Point Defects and Diffusion, by C.P. Flynn, Oxford University Press (1972).
Chemical Kinetics of Solids, by H. Schmalzried, VCH, Weinheim, New York (1995).
Physical Chemistry of Ionic Materials: Ions and Electrons in Solids, by J. Maier, Wiley, Chichester (2004).

Mass Transfer in Fluids

An Introduction to Transport Phenomena in Materials Engineering, 2nd ed., by D.R. Gaskell, Momentum Press (2012).
Transport Phenomena, 2nd ed., by R.B. Bird, W.E. Stewart and E.N. Lightfoot, Wiley, New York (2007).
Estimated Viscosities and Thermal Conductivities of Gases at High Temperatures, by R.A. Svehla, NASA Technical Report R-132, NASA-Lewis, Cleveland, OH (1961).

Mechanical Behaviour of Scales

Protective Oxide Scales and their Breakdown, by M. Schütze, Institute of Corrosion and Wiley, Chichester (1997).
Mechanical Properties of Protective Oxide Scales, Special Issue of Mater. High Temp., 12 (1994).

REFERENCES

[1] O. Kubaschewski, C.B. Alcock, P.J. Spencer, Metallurgical Thermochemistry, sixth ed., Pergamon Press, Oxford, 1993.
[2] I. Barin, G. Platzki, Thermochemical Data of Pure Substances, VCH, Weinheim, 1995.
[3] JANAF Thermochemical Data, Army-Navy-Airforce Thermochemical Panel, Dow Chemical Co., Midland, MI, 1962−1963.
[4] S. Mrowec, K. Przybylski, High temp, Mater. Proc. 6 (1984) 1.
[5] S.R. Shatynski, Oxid. Met. 13 (1979) 105.
[6] C. Wagner, Thermodynamics of Alloys, Addison-Wesley, Reading, MA, 1952.
[7] J.R. Manning, Diffusion Kinetics of Atoms in Crystals, Van Nostrand, Princeton, NJ, 1968.
[8] R.E. Howard, A.B. Lidiard, Rep. Prog. Phys. 27 (1964) 161.
[9] L. Onsager, Phys. Rev.., 37, 405; 38, 2265 (1931).
[10] S.R. de Groot, Thermodynamics of Irreversible Processes, North Holland, Amsterdam, 1952.
[11] I. Prigogine, Introduction to Thermodynamics of Irreversible Processes, C.C. Thomas, Springfield, IL, 1955.
[12] J.S. Kirkaldy, D.J. Young, Diffusion in the Condensed State, Institute of Metals, London, 1987.
[13] P.G. Shewmon, Diffusion in Solids, second ed., Minerals, Metals and Materials Society, Warrendale, PA, 1989.
[14] W. Schottky, in: W. Schottky, Fr. Viewig (Eds.), Halbleiterprobleme, vol. 4, 1958. Braunschweig.
[15] N.F. Mott, R.W. Gurney, Electronic Processes in Ionic Crystals, Clarendon Press, Oxford, 1940.
[16] C.A. Wert, C. Zener, J. Appl. Phys. 21 (1950) 5.
[17] F. Seitz, Acta Cryst. 3 (1950) 355.
[18] A.B. Lidiard, Phil. Mag. 46 (1955) 1218.
[19] M.J. Dignam, D.J. Young, D.W.G. Goad, J. Phys. Chem. Solids 34 (1973) 1227.
[20] D.J. Young, J.S. Kirkaldy, J. Phys. Chem. Solids 45 (1984) 781.
[21] L.C. Brown, J.S. Kirkaldy, Trans. AIME 230 (1964) 223.
[22] J. Nesbitt, J. Electrochem. Soc. 136 (1989) 1518.
[23] D.P. Whittle, D.J. Young, W.W. Smeltzer, J. Electrochem. Soc. 123 (1976) 1073.
[24] W.W. Smeltzer, D.P. Whittle, J.Electrochem. Soc. 125 (1978) 1116.
[25] A. Smigelskas, E. Kirkendall, Trans. AIME 171 (1947) 130.
[26] L.S. Darken, Trans. AIME 175 (1948) 184.
[27] G.S. Hartley, J. Crank, Trans. Faraday Soc. 45 (1949) 801.
[28] H.S. Carslaw, J.C. Jaeger, Conduction of Heat in Solids, Clarendon Press, Oxford, 1959.
[29] J. Crank, The Mathematics of Diffusion, Oxford University Press, 1970.

[30] L. Boltzmann, Ann. Phys. 53 (1894) 960.
[31] C. Matano, Jpn. Phys 8 (1933) 109.
[32] M.A. Dayananda, in: H. Mehrer (Ed.), Diffusion in Metals and Alloys, Landolt and Bernstein, vol. 26, Springer-Verlag, Berlin, 1991, p. 372. Ser. III.
[33] F.S. Pettit, J.B. Wagner, Acta Met 12 (1964) 35.
[34] D.J. Young, M. Cohen, J. Electrochem. Soc 124 (1977) 775.
[35] D.R. Gaskell, An Introduction to Transport Phenomena in Materials Engineering, Macmillan, New York, 1992.
[36] D. Enskog, Arkiv, Met. Astronom. Fyz 16 (1922) 16.
[37] S. Chapman, T.G. Cowling, The Mathematical Theory of Non-uniform Gases, Cambridge University Press, 1939.
[38] R.A. Svehla, Estimated Viscosities and Thermal Conductivities of Gases at High Temperatures, NASA Technical Report R-132, NASA Lewis, Cleveland, OH, 1961.
[39] V.H.J. Lee, B. Gleeson, D.J. Young, Oxid. Met 63 (2005) 15.
[40] X.H. Abuluwefa, R.I.L. Guthrie, F. Ajersch, Oxid. Met 46 (1996) 423.
[41] J. Stringer, Corros. Sci. 10 (1970) 513.
[42] S. Taniguchi, Trans. ISIJ 25 (1985) 3.
[43] F.H. Stott, A. Atkinson, Mater. High Temp 12 (1994) 195.
[44] H.E. Evans, Int.Mater. Rev. 40 (1995) 1.
[45] M. Schütze, Protective Oxide Scales and Their Breakdown, Institute of Corrosion and Wiley, Chihester, 1997.
[46] N.B. Pilling, R.E. Bedworth, J. Inst. Met 29 (1923) 529.
[47] D.J. Baxter, K. Natesan, Rev. High Temp. Mater. 5 (1983) 149.
[48] P. Kofstad, High Temperature Corrosion, Elsevier Applied Science, London, 1988.
[49] D.A. Srolowitz, T.A. Ramanarayanan, Oxid. Met 22 (1984) 133.
[50] P. Hancock, R.C. Hurst, in: M.G. Fontana, R.W. Staehle (Eds.), Advances in Corrosion Science and Technology, vol. 4, Plenum, New York, 1974, p. 1.
[51] W. Christ, A. Rahmel, M. Schütze, Oxid. Met 31 (1989) 1.
[52] R.E. Pawel, J.V. Cathcart, J.J. Campbell, J. Electrochem. Soc. 110 (1963) 551.
[53] J. Litz, A. Rahmel, M. Schorr, Oxid. Met 30 (1988) 95.
[54] N. Belen, P. Tomaszewicz, D.J. Young, Oxid. Met 22 (1984) 227.
[55] J.K. Tien, J.M. Davidson, in: J.V. Cathcart (Ed.), Stress Effects and the Oxidation of Metals Proc. TMS-aime Fall Meeting, TMS-AIME, New York, 1975, p. 200.
[56] F.R.N. Nabarro, in: Rep. Conf. On the Strength of Solids, Physical Society, London, 1948, p. 15.
[57] C. Herring, J. Appl. Phys. 21 (1950) 437.
[58] R.L. Coble, J. Appl. Phys. 34 (1963) 1679.
[59] R.F. Tylecote, J. Iron Steel Inst. 196 (1960) 135.
[60] J. Robertson, M.I. Manning, Mater. Sci. Technol. 6 (1990) 81.
[61] J.K. Tien, J.M. Davidson, Adv. Corros. Sci. Technol. 7 (1980) 1.